Determination of Forced Convection Effects on the Response of Membrane-Based Ion-Selective Electrodes via Numerical Solution to the Navier-Stokes-Nernst-Plank-Poisson Equations

Austin J. Andrews*,Philippe Bühlmann † and Christopher J. Hogan ‡

Ion selective electrodes (ISEs) enable measurements via the build-up of a phase boundary potential at the surface of a sensing membrane. While a framework exists to understand the performance of ISEs in stagnant samples, the influences of fluid flow on ISEs is less studied. We model the transport of charged ions in solution occurring near interfaces between ISE membranes and aqueous samples when subject to an external flow. We developed a numerical model extending the Pressure-Implicit with Splitting of Operators (PISO) algorithm to incorporate the Navier-Stokes-Nernst-Plank-Poisson system of equations. We find that external flow distorts the aqueous side of the formed double layer at the ISE membrane and aqueous sample interface, leading to an increase in the phase boundary potential. The change in potential is shown to be a function of a novel set of dimensionless numbers, most notably the Debye Length Reynolds number, i.e., the Reynolds number with the Debye Length as the system dimension.

I. Introduction

The transport of dilute, charged species via both hydrodynamic and electrostatic forces governs a variety of engineered systems, including but not limited to charged particle transport in aerosols[1] and their collection in electrostatic precipitators [2], flow batteries [3], desalination processes [4], and ion-selective electrodes (ISEs) [5]. In many of these instances, in particular the latter, charged species transport is not only affected by external and internal electric fields, but also through the unequal partitioning of charged species (solutes) at phase boundaries. Unequal partitioning leads to charge separation at the interface and formation of an electric double layer; this ultimately leads to a measurable potential difference. For ISEs, the potential difference arises at the interface of the ISE membrane and an aqueous solution that contains the analyte ion of interest. Formation of this phase boundary potential allows for the measurement of the concentration of this analyte ion. Considerable effort has been dedicated to the design of specific membrane materials to obtain selectivity for various different target ions [6]. In general, ISE membranes comprise (i) a polymeric membrane matrix that provides the membrane with mechanical robustness, (ii) the analyte ion either

*Graduate Research Assistant, University of Minnesota, 111 Church St SE, Minneapolis, MN 55455
†Professor, University of Minnesota, 207 Pleasant St SE, Minneapolis, MN 55455
‡Professor, University of Minnesota, 111 Church St SE, Minneapolis, MN 55455

in a free form or in the form of a complex with an ion-selective receptor (usually referred to as ionophore), as well as a (iii) counter ion (referred to as ionic site) that is either covalently attached to the matrix polymer or has such a high hydrophobicity that leaching into aqueous samples is negligible. A phase boundary potential forms because the analyte ion and counterions differ in their free energies of transfer from the sample into the membrane phase [7]. While ISE theory typically assumes local equilibrium at the interface of the sample and membrane phase, the transport of ions between the two phases both by diffusion and convection may influence the magnitude of the phase boundary potential. A well-known illustration for this are the zero-current transmembrane ion fluxes that often determine the lower detection limits of ISEs [8]. Also, through experimental measurements of membrane resistance, Dlugolecki et al. found that external fluid flow may influence the electric double layer particularly for low solution concentrations [9]. However, the effect of fluid flow on phase boundary potentials has only been qualitatively explored in prior work, mainly because explicit computation of ion transport accounting for fluid flow requires numerical solution to the Navier-Stokes-Nernst-Plank-Poisson (NS-NPP) set of equations, which combine conservation of mass and momentum for fluid flow with mass conservation of each charged species, with Poisson's equation for the electric potential. This is a complex set of equations with extensive coupling, and is a stiff system of equations.

Modeling of ISEs presents unique challenges due to the need to account for ion exchange at the ISE membrane and aqueous sample interface. Ions differentially transport across membrane interfaces primarily due to differences in affinity for the sample and the membrane phase and may be further altered by binding of the analyte ion to ion receptors in the membrane phase [10]. Prior work conducted for modeling ISE systems has hence more frequently examined numerical solutions to the NPP equations, i.e. the Nernst-Planck-Poisson (NPP) equations, which do not consider fluid flow [11–15]. In these studies, there has been two primarily employed methods to handle the phase boundary interface. First, coupling between phases has been accomplished using two separate simulation domains, with the Chang-Jaffe boundary condition [13, 16] at the interface, which relates the flux across the ISE membrane and aqueous sample interface to a reversible 1st order reaction. Second, interface mass transfer has been modeled by generalizing ion transport to include gradients in ion activity [14], allowing for a singular domain, keeping track of spatial variations in the affinity of ions for the two contacting phases.

There have been studies exploring the effects of fluid flow on ion motion within flow-through ion exchange membranes that are used for electrodialysis (ED)[17–22]. In these studies, the NS-NPP equations were applied, but their their use was limited to the aqueous phase, focusing on electroconvection and instabilities occurring from an applied external voltage. The ion concentrations at the phase boundaries were determined by boundary conditions such as specifying a fixed ion concentration[18] or modeling by Butler-Volmer kinetics[19]. In contrast to electrodialysis systems, ISE sensing devices are rarely operated with an applied external potential and hence ion currents in ISEs are usually near zero. Instabilities that lead to electroconvection generally occur when the ion currents are beyond the ohmic region [23]. Therefore, it is expected that fluid instabilities arising in ED cells are absent from the problems considered

in this study, where no external potential is applied.

As understanding the potential response is critical to the design and implementation of ISEs as sensing devices, it is important to know if and when external flow affects the response of such devices, and to probe fundamental behavior of systems with coupled ion mass transfer, fluid flow, and electrostatics at interfaces. In addition to applications in electrodialysis, the NS-NPP equations have been solved to predict the behavior of nanopore sensors [24], model electrostatic precipitators [25], and examine EHD-assisted droplet formation (i.e. electrosprays) [26], among others. As alluded to above, numerical solutions of these sets of equations has been particularly difficult, and the choice of numerical schemes is crucial to ensure accuracy and convergence [27]. As the aforementioned works utilize different numerical schemes, we believe there is still a need to advance NS-NPP solution schemes and to examine fundamental NS-NPP transport solutions near phase boundaries. Towards this end, here we develop an NS-NPP solution scheme to model ion transport and the evolution of the phase boundary potential in systems that approximate ISEs and which also resemble classical laminar flow boundary layers. Described in the subsequent section, the numerical solution scheme developed utilizes the finite volume method for spatial discretization and extends Issa's Pressure-Implicit with Splitting of Operators (PISO) [28] solution algorithm for incompressible flows to include coupling between the NS and NPP equations. The NPP equations are solved using Hagelaar's method [29]. A high order embedded Runge-Kutta(RK) method with variable step size is used for time discretization. Development of this method was conducted using the open source package OpenFOAM [30]. Algorithm validation is performed via comparison to a series of analytical solutions, classical solutions, and prior experiments. Subsequently, the algorithm is applied to examine the phase boundary potential developed across a membrane while simultaneously a laminar boundary layer develops (i.e., the Blasius solution augmented by mass transfer of charged species). We show that the dimensionless phase boundary potential is positively correlated to increased fluid flow and decreased ion diffusion rates.

II. Theory and Solution Scheme

A. Governing Equations

To model the effects of fluid flow on ion transport in ISE systems, with the assumptions of incompressible (assuming low fluid Mach number), laminar (low fluid Reynolds number) and isothermal flow, the Navier-Stokes equations (Equation 1a and Equation 1n), Nernst-Planck equation (Equation 1d), and Poisson equation (Equation 1c) are employed

and are defined as:

$$\nabla \cdot \vec{U} = 0 \tag{1a}$$

$$\frac{\partial \vec{U}}{\partial t} + \vec{U}\nabla \cdot \vec{U} = -\nabla \frac{P}{\rho_f} + \nu \nabla^2 \vec{U} + \nabla \cdot \nu[(\nabla \vec{U})^T - \frac{2}{3}(\nabla \vec{U})] + \frac{f_e}{\rho_f} \tag{1b}$$

$$\nabla \cdot \epsilon \nabla \phi = \sum_{i=1}^{i=n} F c_i z_i \nabla \phi \tag{1c}$$

$$\frac{\partial c_i}{\partial t} + \nabla \cdot (c_i[\vec{U} + z_i \frac{F D_i}{RT} \nabla \phi + \Theta]) = \nabla \cdot D_i \nabla c_i \tag{1d}$$

$$\Theta = \frac{D_i(1 - k_i)}{\alpha + k_i(1 - \alpha)} \nabla \alpha \tag{1e}$$

where $\vec{U}$ is the fluid velocity, P is the hydrodynamic pressure, ρ_f is the fluid density, ν is the fluid kinematic viscosity, ϕ is the electrostatic potential, f_e is the electrostatic body force, ϵ is the permittivity, F the Faraday constant, c_i the molar concentration of ion species i, z_i the charge of species i, D_i the ion diffusion coefficient, R the universal gas constant, T the temperature of the surrounding medium, k_i is the single ion partition coefficients, and α the membrane mass fraction, differentiating between the membrane phase ($\alpha = 1$) and aqueous ($\alpha = 0$). The third term on the right hand side of Equation 1b is equal to zero when the flow is incompressible, i.e. Equation 1a is satisfied, and is added for numerical stability [31]. The body force term f_e represents the drag force imparted onto the fluid from the movement of charged particles and is defined as $f_e = \sum_{i=1}^{i=n} F c_i z_i \nabla \phi$. This body force is a simplification of the more general Lorenz force [32] by disregarding effects from magnetic fields, which is commonly done for ions in solution. To improve stability of the numerical solution and coupling between the membrane and water phase, the simulation domain is monothetic with ion selectivity modeled through single ion partition coefficients and the mass transfer model from Haroun et al. represented by Θ in Equation 1e [33]. Originally formulated to enforce non equal partitioning of gases (Henry's law), Haroun's mass transfer model ensures mass conservation at phase boundaries and enforces the jump condition that occurs with non-equal partitioning of ions, i.e., the ratio of ions present in the water (c_{aq}) and membrane phases (c_{mem}) are non unity $\frac{c_{aq}}{c_{mem}} = k \neq 1$ [33]. The additional flux (Θ), referred to as the "solubility flux", acts to counteract the nonphysical diffusive flux that would arise from a concentration jump at interfaces, where $\nabla \alpha \neq 0$. At thermodynamic equilibrium, when $c_{aq} = k c_{mem}$, the solubility flux (Θ) is equal in magnitude to the diffusive flux at the interface when central discretization schemes are used regardless of the mesh size near the interface [33]. This interface model is similar to the traditionally used Chang-Jaffe boundary conditions assuming diffusion limited surface reactions, but with the added benefit of a singular domain to describe the NPP equations. To our knowledge, this approach, which has been successfully employed in gas partitioning into liquids [34, 35], has not employed in conjunction with the NS-NPP equations previously, and has not been employed in examining ion selectivity across phase boundaries. We also note that here binary values of α are employed, but more general α can be treated as a phase fraction and the

Table 1 Mathematical description of the boundary conditions as labeled in 1a with n representing the face normal direction and I the identity matrix. The subscripts f and p signify the value at the boundary face and neighboring cell, respectively.

Boundary	Ions (c_i)	Potential (ϕ)	Velocity ($\vec{U}$)	Pressure (P)
1	$\frac{\partial c_i}{\partial n}_f = 0$	$\frac{\partial \phi}{\partial n}_f = 0$	$\vec{U}_f = (1,0,0)$	$\frac{\partial P}{\partial n}_f = 0$
2	$\frac{\partial c_i}{\partial n}_f = 0$	$\frac{\partial \phi}{\partial n}_f = 0$	$\frac{\partial \vec{U}}{\partial n}_f = 0$	$\frac{\partial P}{\partial n}_f = 0$
3	$\frac{\partial c_i}{\partial n}_f = 0$	$\frac{\partial \phi}{\partial n}_f = 0$	$\frac{\partial \vec{U}}{\partial n}_f = 0$	$P_f = 0$
4	$\frac{\partial c_i}{\partial n}_f = 0$	$\frac{\partial \phi}{\partial n}_f = 0$	$\vec{U}_f = \frac{1}{2}(\vec{U}_p + (I - 2nn^T)\vec{U}_p)$ *	$\frac{\partial P}{\partial n}_f = 0$
5	$\frac{\partial c_i}{\partial n}_f = 0$	$\frac{\partial \phi}{\partial n}_f = 0$	$\vec{U}_f = (0,0,0)$	$\frac{\partial P}{\partial n}_f = 0$
6	$\frac{\partial c_i}{\partial n}_f = 0$	$\frac{\partial \phi}{\partial n}_f = 0$	–	–
Membrane-Water Interface	–	–	$\vec{U}_f = (0,0,0)$	$\frac{\partial P}{\partial n}_f = 0$

approach applied here can be extended to mixtures unlike the Chang-Jaffe boundary condition.

B. Domain and Boundary Conditions

In lieu of modeling a complete ISE sensor geometry, we base our model off of classical boundary layers with a leading edge, as the fluid flow and shear stress in the absence of ion migration and electrostatic body forces are well known in this scenario. The specific computational domain employed is a 2D representation of flow over a flat membrane and is shown in Figure 1. Here the numerical solution of the NS equations (U and P) is restricted to only the white region labeled "Water" in 1a. The electric potential (ϕ), a continuous variable, is solved for in both the aqueous phase and the membrane phase (shaded gray in 1b) without distinction between phases, as we modeled both phases with the same electrical permittivity. The species concentration (c_i) is also solved for in both the aqueous phase and membrane phase, but accounting for partitioning at the water-membrane interface via Haroun's solubility flux approach [33]. The same computational mesh was used for both the global domain, comprising of the aqueous and membrane phase, as well as the aqueous phase. Therefore, the fluid properties solved within the separate water subdomain are easily mapped to the global domain for solution of Equation 1d. In Figure 1a, each boundary is labeled and the corresponding boundary conditions may be found in Table 1. The domain was made sufficiently large such that the effect of boundary conditions, namely the zero gradient condition on the potential, would not affect the results near the ISE membrane and aqueous sample interface. The computational mesh was designed using hanging nodes and successive refinement to ensure high spatial resolution near the membrane and fluid interface without compromising the overall simulation cost, particularly as the unsteady nature of this simulation and highly coupled equations make computational cost high. The mesh selected had $4.3 \cdot 10^5$ hexahedral cells and is shown in Figure 1b.

*The boundary condition at Boundary 4 is commonly referred to as the symmetry condition. The implementation of this boundary condition for multi-dimensional variables such as U is the mean of the adjacent cell and the mirror image produced by the Householder transformation. [36]

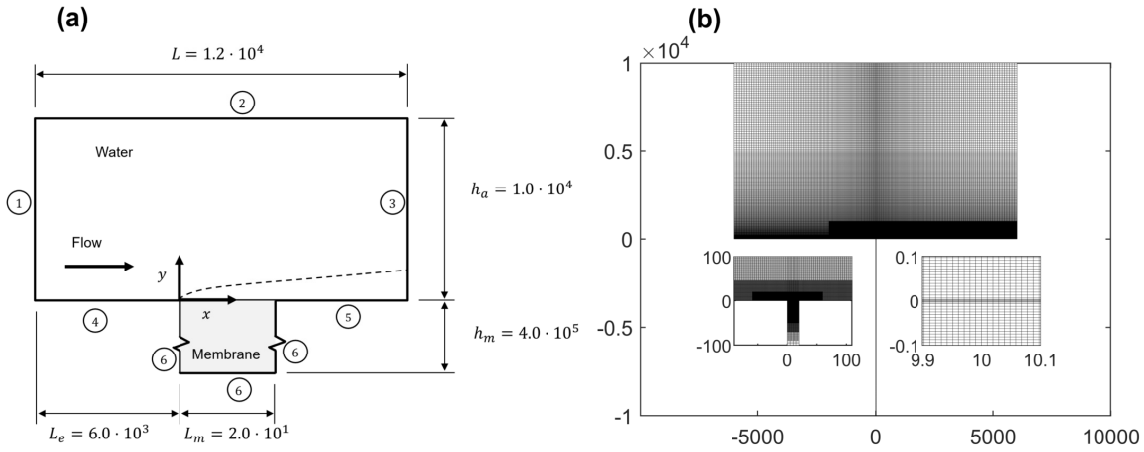

Fig. 1 Schematic of the computational domain of a liquid flow over an immiscible membrane phase. (a) Dimensions and labeled boundaries, with more details provided in Table 1. (b) Computational mesh used in this study, with insets providing higher magnification of the ISE membrane and aqueous sample interface. All units presented in this figure are dimensionless, with the dimensionless length scale defined as $x^* = \frac{xU_0}{\nu}$. More information about the non-dimensionalization procedure can be found in the Theory and Solution Scheme section.

C. Numerical Solution Scheme

A custom C++ program was developed to solve Equations 1a-e using the finite volume method and open source library OpenFOAM. This library abstracts many of the aspects of finite volume discretization and subsequent matrix construction and numerical solution. This allows developers to focus on higher level solution algorithms and add additional transport equations such as those present in the NS-NPP equations. To solve the coupled system of Equations 1a-e for the dependant variables $U, P, \phi, c_0, c_1, ...$ and c_i, a modification to the PISO algorithm [28] to include the NPP equations along with an embedded singly-diagonal implicit Runge-Kutta(SDIRK) [37] time discretization is used. Time steps are varied using a PPID time step controller[38] with a desired normalized numerical solution error of $1 \cdot 10^{-6}$. More information on the specific implementation of time step control is included in the supporting information. Within the PISO algorithm, a sub loop for the Nernst-Planck equation coupling with the Poisson equation is solved using the semi-implicit algorithm from Hagelaar et al. [29]. The modified PISO algorithm implemented along with the implementation of Hagelaar's method is shown in Algorithm 1.

To explain the modifications to the PISO algorithm, the notation used is consistent to what is largely used by the OpenFOAM community and can be found in detail within Jasak's PhD thesis [39]. For brief explanation of the notation, the H operator includes all off diagonal components of the discretized momentum equation (Equation 1b) along with any explicit source terms arising from boundary conditions and time discretization methods. The a coefficient represents the diagonal components of the discretized momentum equation. All iterative values, n, i, j, k in Algorithm 1 use superscripts with parenthesis () to indicate iteration steps, and brackets [] to indicate the SDIRK stage. The

algorithm begins by calculating the fluid variables (U and p) with the standard PISO algorithm implementation as is done within OpenFOAM's solver pisoFOAM with the addition of the electrostatic body force, which is calculated explicitly by values from previous iterations. Following the computation of U and p, the electrostatic potential and species concentrations are solved using Hagelaar's algorithm without update to fluid variables U and p. The Algorithm ends with another iteration of the PISO algorithm, but this time with updated values for ϕ and c. The Algorithm was structured such that the variables with the strongest coupling, such as the pairs U and p and ϕ and c, have adequate convergence before incorporating the weaker, but still prevalent, body force term that couples the fluid variables to the species transport. The "stop" condition for each loop is based on convergence of the resulting linear systems for Equations 1a-e. The convergence is determined based on the L_1 norm of the matrix residuals and is defined as $r = \frac{1}{\sum(|Ax - A\bar{x}| + |b - A\bar{x})} \sum |b - Ax|$ where A and b are the coefficient matrix and source term produced from the finite volume and time discretization of the variable x with $\bar{x}$ representing the average value of x. Convergence was determined when the L_1 norm was at or bellow $1 \cdot 10^{-6}$ before exiting the iteration loops presented in Algorithm 1.

For the spatial discretization, built-in functionality of OpenFOAM's matrix constructors were employed. For all transport equations, divergence operators were discretized using 1st order upwind methods, while gradient operators used Gaussian integration with 2nd order linear interpolation without non-orthogonal or skewness corrections. This solver uses a custom time discretization following the work of Dalessandro et al.[40] for incorporating SDIRK methods into OpenFOAM. The specific method used was a 3rd order 3 stage embeded SDIRK method with a 2nd order error estimator from Alexander[37]. For the special case of solving the Poisson equation with only Neumann boundary conditions (electric field equal to zero on all boundaries), the fixed point method [41] is applied. Here the compatibility condition and fixed point value are enforced by modifying the resulting matrix equation from the discretization of Equation 1c by solving the modified linear system $A^{'}x = b^{'} - \bar{b^{'}}$ where $A' = A + A(i,i)$ and $b^{'} = b + A(i,i)\phi_{ref}$. Here i represents the cell location of the fixed value (ϕ_{ref}) and $\bar{b^{'}}$ is the average of the matrix source term $b^{'}$. For further details of implementation, the complete code is linked in the supporting information.

The order of the numerical solution was inspired by Oliveira's PISO extension for buoyancy driven flows [42] where similarly the NS equations are modified to include a body force derived from a scalar transport equation, in Oliveira's case the heat equation and here the Poisson equation, which in turn is influenced by the ion transport equation. While the exact solution order may affect stability and convergence rates, the proposed algorithm was deemed suitable for the present study and has been validated with a series of analytical, experimental and prior numerical studies. The first comparison is to experimental measurements of the velocity profile in an electrostatic precipitator, where the velocity is influenced by the electrostatic body force [43] and hence its determination requires solution to the NS-NPP set of equations. The second is a comparison to Schönke's [44] analytical solution for the NPP set of equations, testing our ability to recover solutions with coupled mass transfer and electrostatics. The third is recovery of the classical Blasius solution for boundary layers of a flat plate. In the absence of electrostatic effects, for the geometry tested here (Figure

Algorithm 1 Segregated solver for the numerical solution to the coupled NS-NPP equations.

$n \leftarrow 1$
while RK loop **do**
  $i \leftarrow 1$
  while U,P,ϕ,c_0,c_1,...c_i are not converged **do**
    $j \leftarrow 1$
    while U,P are not converged **do**
      $U^{(j+1)} \leftarrow \frac{\partial U}{\partial t}^{[n]} + U^{(j)}\nabla \cdot U^{(j+1)} = -\nabla P^{(j)} + \nu\nabla^2 U^{(j+1)} + \nabla\frac{\phi^{(i)}}{\rho}\sum_{s=1}^{S} e z_s c_s^{(i)}$ ▷ Solve Predictor step
      $P^{(j+1)} \leftarrow \nabla \cdot \frac{1}{a}\nabla P^{(j+1)} = \nabla \cdot \frac{H(U^{(j+1)},\phi^{(i)},c_i^{(i)})}{a}$ ▷ Solve Pressure Equation
      $U^{(j+2)} \leftarrow \frac{H(U^{(j+1)},\phi^{(i)},c_i^{(i)})}{a} - \frac{1}{a}\nabla P^{(j+1)}$ ▷ Corrector Step
      $j \leftarrow j + 1$
    end while
    $k \leftarrow 1$
    while ϕ,c_0,c_1,...c_i are not converged **do**
      if j == 1 **then**
        $\beta \leftarrow \epsilon + \sum_{s=1}^{S} z_s^2 \delta t c_s^{[n]}$
        $\phi^{(k+1)} \leftarrow \nabla \cdot \beta\nabla\phi^{(k+1)} = \sum_{s=1}^{S} z_s c_s^{[n]} F + \sum_{s=1}^{S} F z_s \delta t(\frac{\partial c_s}{\partial t}^{[n]} - z_s c_s^{[n]} \frac{FD_s}{RT}\nabla\phi^{[n]})$ ▷ Voltage Predictor
      else
        $\phi^{(k+1)} \leftarrow \nabla \cdot \epsilon\nabla\phi^{(k+1)} = \sum_{s=1}^{S} z_s c_s^{[n]} F$
      end if
      $c^{(k+1)} \leftarrow \frac{\partial c}{\partial t}^{[n]} + \nabla \cdot (c_i^{(k+1)}[z_i \frac{FD}{RT}\nabla\phi^{(k+1)} + U^{[n]} + \frac{D_i(1-k_i)}{\alpha+k_i(1-\alpha)}\nabla\alpha]]) = \nabla \cdot D\nabla c_i^{(k+1)}$
      $k \leftarrow k + 1$
    end while
    $j \leftarrow 1$
    while U,P are not converged **do**
      $U^{(j+1)} \leftarrow \frac{\partial U}{\partial t}^{[n]} + U^{(j)}\nabla \cdot U^{(j+1)} = -\nabla P^{(j)} + \nu\nabla^2 U^{(j+1)} + \nabla\frac{\phi^{(i+1)}}{\rho}\sum_{s=1}^{S} e z_s c_s^{(i+1)}$ ▷ Solve Predictor step
      $P^{(j+1)} \leftarrow \nabla \cdot \frac{1}{a}\nabla P^{(j+1)} = \nabla \cdot \frac{H(U^{(j+1)},\phi^{(i+1)},c_i^{(i+1)})}{a}$ ▷ Solve Pressure Equation
      $U^{(j+2)} \leftarrow \frac{H(U^{(j+1)},\phi^{(i+1)},c_i^{(i+1)})}{a} - \frac{1}{a}\nabla P^{(j+1)}$ ▷ Corrector Step
      $j \leftarrow j + 1$
    end while
    $i \leftarrow i + 1$
  end while
  $n \leftarrow n + 1$
end while

1), simulations recover the Blasius solution, showing that the flow modeled is a viscous boundary layer flow in the developing region. Validation results can be found in the supplemental material. Further validations more specific to ISEs are discussed in the Results and Discussion section [11]. Simulations were run on a Minnesota Supercomputing Institute (MSI) cluster utilizing 8 cores for each simulation and requiring roughly 120 hours of run time for each case noted in the subsequent section.

D. Non-Dimensionalization and Test Cases

To reduce the number of independent parameters affecting fluid flow and transport of charged ions in solution, we adopt a non-dimensionalization conventionally utilized in studying boundary layer formation from external flow of a viscous fluid over a surface [45]. We define the non-dimensional length scale as $x^* = \frac{xU_0}{\nu}$ where U_0 is the bulk fluid velocity and x the spatial dimension, the non-dimensional time scale as $\tau = \frac{t\nu}{U_0^2}$ and the non-dimensional velocity as $U^* = \frac{U}{U_0}$. This variable transformation fixes fluid behavior to problem geometry (x^*) and time scale (τ), allowing for examination of other transport phenomena, such as ion motion within the formed fluid boundary layer, with fixed fluid characteristics. We correspondingly define the non-dimensional potential as $\phi^* = \phi\frac{Fc_0}{\rho_f U_0^2}$ where c_0 is the reference ion concentration and the non-dimensional concentration as $c^* = \frac{c}{c_0}$. This combination of fluid and electrochemical variable transformations leads to the non-dimensionalization of Equations 1a-e as:

$$\nabla \cdot \vec{U}^* = 0 \tag{2a}$$

$$\frac{\partial \vec{U}^*}{\partial \tau} + \vec{U}^*\nabla \cdot \vec{U}^* = -\nabla P^* + \nabla^2\vec{U}^* + \nabla \cdot [(\nabla\vec{U}^*)^T - \frac{2}{3}(\nabla\vec{U}^*)] + \sum_{i=1}^{i=n} c_i^* z_i \nabla\phi^* \tag{2b}$$

$$\nabla^2\phi^* = \frac{1}{Re_{db}^2\psi_f}\sum_{i=1}^{i=n} c_i^* z_i \tag{2c}$$

$$\frac{\partial c_i^*}{\partial \tau} + \nabla \cdot (c_i^*[\vec{U}^* + z_i\frac{\psi_f}{Sc_i}\nabla\phi^* + \Theta^*]) = \frac{1}{Sc_i}\nabla^2 c_i^* \tag{2d}$$

$$\Theta^* = \frac{1}{Sc_i}\frac{(1-k_i)}{\alpha + k_i(1-\alpha)}\nabla\alpha \tag{2e}$$

$$\tag{2f}$$

where the resulting dimensionless parameters are the fluid kinetic to chemical potential energy ratio $\psi_f = \frac{\rho_f U_0^2}{c_0 RT}$, the ion Schmidt number $Sc = \frac{\nu}{D}$ and the Debye-length Reynolds number $Re_{db} = \frac{U_0\lambda_{db}}{\nu}$ with the Debye length $\lambda_{db} = \sqrt{\frac{\epsilon RT}{F^2 c_o}}$. The Debye-length Reynolds number determines the relative strength of the fluid flow inertia within one Debye length of the fluid-membrane interface. When Re_{db} is large ($Re_{db} >> 1$), significant changes to ion transport rates, driven by fluid flow, occur in the region most sensitive to changes in electrostatic potential. Conversely, when Re_{db} is small ($Re_{db} << 1$), electrostatic forces dominate ion transport, i.e., convection has little influence on transport at the membrane interface. As will be seen in later sections, this parameter will be paramount to exploring the effects

of fluid flow on partitioning of ions across the membrane-water interface. Dimensionless numbers associated with membrane and ion transport found in prior work [11] (i.e., when solving the NPP equations) can be defined from this set of non-dimensional parameters, including the dimensionless potential $\psi_f \phi^* = \phi \frac{F}{RT}$, dimensionless length scale $\frac{x^*}{Re_{db}} = \frac{x}{\lambda_{db}}$ and dimensionless time scale $\frac{\tau}{ScRe_{db}^2} = \frac{tD}{\lambda_{db}^2}$. These dimensionless ratios will be used in the subsequent sections for analyzing the mass transfer of ions and associated changes in the potential across the membrane-water phase boundary.

A series of simulations where preformed varying Sc, Re_{db} and ψ_f for a binary salt solution. To accomplish this using the code developed for Equations 1a-e, variables ν, c_0, U and ρ_f were set to 1 m^2s^{-1}, 1 mol m^{-3}, 1 m s^{-1} and 96485 kg m^{-3} (having the same magnitude as Faraday's constant) respectively. The remaining three variables, i.e., D_i, ϵ and T, were modulated to represent Sc, Re_{db} and ψ_f. For each case the non-dimensional ion concentration (c^*) was initialized as a constant value of 1.0 in both the membrane and water phases for the cation (+1 charge) and anion (-1 charge). Similarly, the non-dimensional velocity (U^*) was set to a magnitude of 1 with a direction parallel to the plate. For a test of this model, it was assumed here that the ion diffusion coefficient varied neither in space or phase and that it was the same between the anion and cation. Permittivity (ϵ) was also held constant throughout the domain irrespective of phase. For all cases the single ion partition coefficients (k_i) were held constant with a value of 2 (hydrophilic) for the cation and 0.5 (hydrophobic) for the anion, similar to parameters used by [11] in examining transport across an interface. To ensure accurate capture of the thin double layer, the mesh was designed to have a cell thickness at the phase boundary of no more than $0.02\lambda_{db}$ when $Re_{db} = 0.1$, noting that the mesh and dimensions of the membrane are scaled based on fluid properties and not the Debye length. To test mesh quality, a secondary mesh with resolution of $1.5 \cdot 10^6$ hexahedral cells and fa phase boundary cell thickness of no more than $0.01\lambda_{db}$ was run for two selected cases ($Re_{db} = 1$, $\psi_f = 1$, $Sc = 1000$ and $Re_{db} = 0.1$, $\psi_f = 1$, $Sc = 1000$). The potential between these two mesh resolutions varied no more than 1% when $\frac{\tau}{ScRe_{db}^2} > 1$. Therefore, the first mesh with $4.3 \cdot 10^5$ cells depicted in Figure 1b was used for the remainder of the study.

III. Results and discussion

In the absence of external flow (i.e, when $Re_{db} = 0$) or when flow is negligible, a double layer is formed and the resulting potential arises from the non-equal partitioning of ions. This potential can be predicted at the $t \rightarrow \infty$ limit by recognizing that, at equilibrium, the electrochemical potential of each ion is the same in both phases. For a binary electrolyte consisting of monovalent ions, this can be formulated to be a function of the single ion partition coefficients, and is defined as [11, 46]

$$\Delta(\psi_f \phi^*) = \frac{1}{2} ln \left(\frac{k_+}{k_-} \right) \tag{3}$$

where k_+ and k_- are the single ion partition coefficients of the cation and anion, respectively. Prior research has shown that Equation 3 accurately describes the phase boundary potential at the $t \rightarrow \infty$ limit when the diffusion potential, often referred to as the Henderson potential, is negligible, i.e., when the partitioning ions have the same diffusion coefficient [11, 47]. To demonstrate this and to provide code validation, we compare the temporal evolution of the phase boundary potential with the expected value obtained from Equation 3 for the case of no-flow. Figure 2a shows that when $tD/\lambda_{db}^2 > 1$ the potential converges to the predicted value from Equation 3. We observe that the evolution of the phase boundary potential is clearly divided into a a dynamic phase for $tD/\lambda_{db}^2 < 1$ and an effectively static phase at $tD/\lambda_{db}^2 > 1$, suggesting that the use of tD/λ_{db}^2, which is equivalent to $\frac{\tau}{ScRe_{db}^2}$, is a well-scaled dimensionless time for these systems and is henceforth used to present temporally-varying results. For additional validation, the ion concentration profiles near the ISE membrane and aqueous sample interface at $tD/\lambda_{db}^2 = 10$ are compared with the results obtained from Zhurov et al. [11] in Figure 2b for the case where $k_+ = 2$ and $k_- = 0.5$. We apply these same partition coefficients here and throughout this study. However, specific to this validation, we employ $Sc = 3.98$ for the cation and $Sc = 1$ for the anion in order to match the conditions from Zhurov et al. The concentration profiles for both the cation and anion in Figure 2b show a high degree of symmetry as in the absence of flow, ion motion is dominated by near interface electric fields and concentration gradients, which are independent between phases for this problem set up. The strong agreement here, demonstrates simulations correctly capture ion diffusive and electrophoretic motion as well as the development of a space-charge induced electrostatic potential field. Additional validations are provided in the supporting information, including comparison to classical boundary layer results, comparison to analytical NPP equation solutions and comparison with experimental electrohydrodynamic flow velocity measurements.

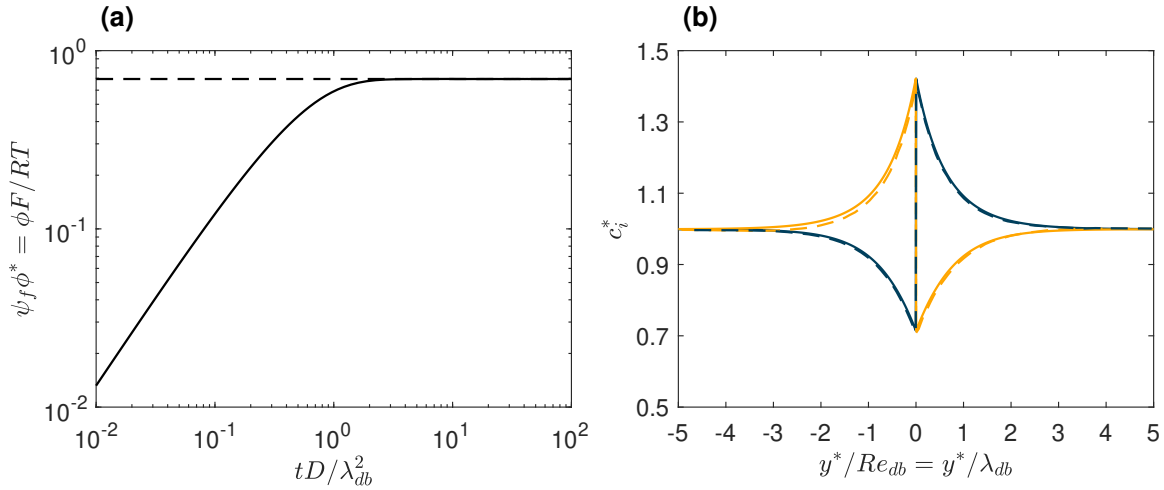

Fig. 2 Results for the no-flow case ($\psi_f = 1$, $Sc = 1000$, $Re_{db} = 0$). (a) Temporal evolution of the phase boundary potential (solid black line) compared to expected potential from Equation 3 (dashed black line). (b) Concentration profiles of Cation (blue) and Anion (yellow) with comparison between the current study (solid) and results from Zhurov et al. [11] (dashed). Quantities where taken from the midpoint location of membrane, $x^* = 5$, with the ISE membrane and aqueous sample interface at $y^* = 0$ and at a time of $tD/\lambda_{db}^2 = 10$. Information on the Domain used refer to Figure 1.

Adding external flow to this system, Figure (3) displays a series of cation and anion concentration maps for variable Debye Length Reynolds numbers, with fixed ψ_f, which is the dimensionless parameterization of ion mobility, and fixed Sc, the dimensionless parameterization of ion diffusivity. The case shown in Figures (3a) (cation) and (3e) (anion), with a $Re_{db} = 0.1$, shows concentration profiles mostly unaffected by external flow; this case is similar to the validation case presentation in Figure 2b. The concentration boundary is confined to the narrow region close to the membrane with near-lateral symmetry. However, with increasing Re_{db}, analogous to the boundary layer formed for similar problems of forced convection on surfaces, fluid flow increases ion concentration gradients near the fluid-membrane interface, particularly at the leading edge, as is evident in Figures (3b-d) and (3f-h), and leads to formation of a growing boundary layer. As Re_{db} tends to unity, fluid flow effects on the boundary are pronounced, with noticeable ion concentration variation at y^*-locations near 1.0, in comparison to the boundary layer in the absence of fluid flow of order 0.01 in thickness.

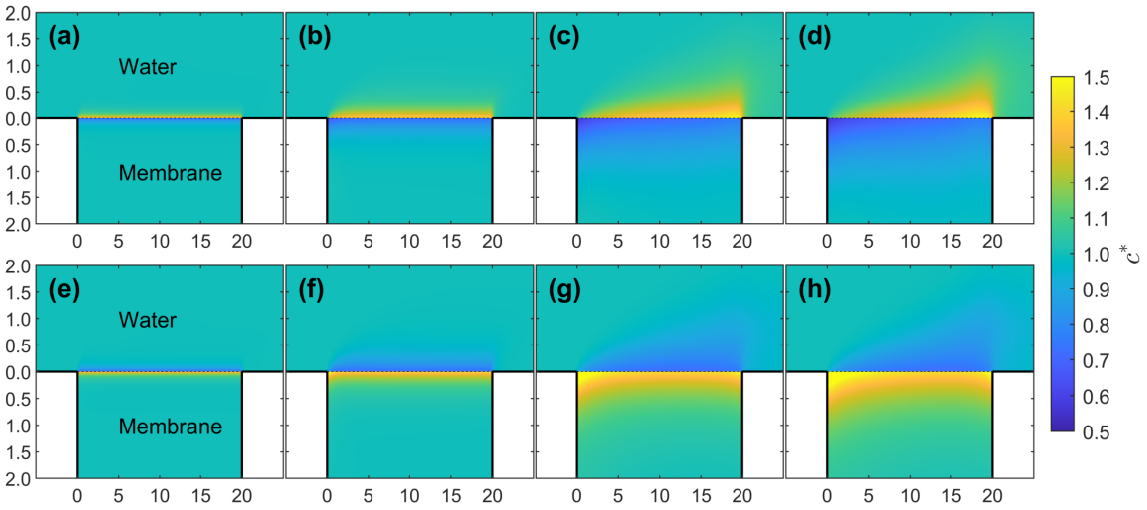

Fig. 3 Spatial distribution of dimensionless ion concentration c_i^* near the ISE membrane and aqueous sample interface at a time of $\frac{\tau}{ScRe_{db}^2} = 10$ for the cations (a-d) and anions (e-h) with single ion partition coefficients of 2.0 (cation) and 0.5 (anion) as well as $\psi_f = 1$ and $Sc = 1000$. From Left to right, varying Re_{db} with $Re_{db} = 0.1$ (a and e),$Re_{db} = 0.3$ (b and f),$Re_{db} = 0.8$ (c and g) and $Re_{db} = 1.0$ (d and h). All spatial dimensions are non-dimensional defined by Equation 2. The black dashed line represents the phase boundary.

The differences between the low flow velocity ($Re_{db} = 0.1$) and high flow velocity cases ($Re_{db} = 1$) are also demonstrated by profile data at $x^* = 5$ as shown in Figure 4a. This x^* location is selected intentionally to be close to the leading edge of the membrane, but sufficiently distal to avoid the influence of edge effects. We specifically plot ion concentration as a function of y-location normalized by the Debye length, which is the product of y^* and Re_{db} in the employed dimensionless framework. The low Re_{db} (dashed lines in Figure 4a) hence leads to concentration boundary layers of length near unity, i.e., similar in thickness to the Debye length. As Re_{db} increases to 1.0 (solid lines in Figure 4a) the encroachment of the fluid boundary layer within 1 Debye length of the interface leads to a small, but

noticeable decrease in the thickness of the charge separation layer in the fluid phase (when normalized by the Debye length). In in Figure 4b we plot the total charge density (dimensionless) as a function of $y^* Re_{db}^{-1}$ across the membrane and aqueous phase, as well as the dimensionless potential ($\psi_f \phi^*$) across the interface. This subtle asymmetry brought about by flow leads a pronounced increase in the potential at distance larger than the Debye length. Insets in Figure 4b nonetheless show that the potential reach a near constant value close the membrane interface (i.e. after several Debye lengths), hence the main effect is to increase the phase boundary potential.

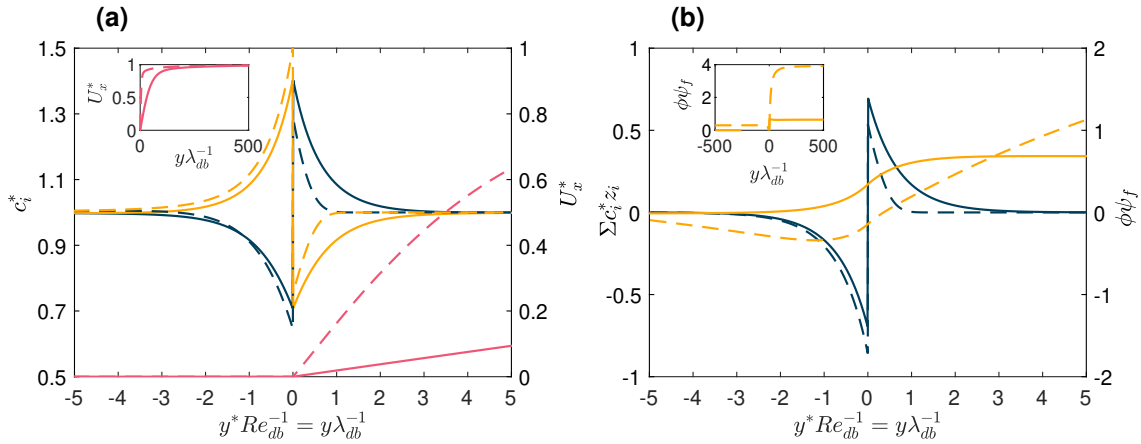

Fig. 4 Quantities of interest at varying $y*$, with the ISE membrane and aqueous sample interface occurring at $y^* = 0$, taken from a location within the membrane, $x^* = 5$, for $\psi_f = 1$, $Sc = 1000$, $Re_{db} = 0.1$ (dashed lines) and $Re_{db} = 1.0$ (solid lines). (a) Dimensionless charge concentration (blue) and dimensionless electric potential $\phi\psi_f$ (yellow) varying over dimensionless length (scaled by Debye length). (b) Dimensionless concentration for cation (blue) anion(yellow) and dimensionless velocity ($U^* = U/U_0$) varying over dimensionless length (scaled by Debye length).

In Figure 5 we plot the temporal evolution (with tD/λ_{db}^2 again as the dimensionless time) of the phase boundary potential for variable combinations of ψ_f and Sc and Re_{db} varying from 0.1-1.0. In all cases, similar to zero flow condition, we observe dynamic and static regions, separated by tD/λ_{db}^2 near unit value. Interestingly at small times, independent of Re_{db}, ψ_f, and Sc. the phase boundary potential increases with tD/λ_{db}^2 scaled to the power of 1, suggesting early time behavior is completely diffusion limited. With increasing Re_{db} in all cases we observe changes in both the dynamic regime and the static regime. In the dynamic regime, the phase boundary potential begins to increase more rapidly at higher Re_{db} for tD/λ_{db}^2 beyond 10^{-1}, with a scaling exponent approaching 1.6 for $Re_{db} = 1.0$, $\psi_f = 1.0$ and $Sc = 1000$, suggesting that fluid flow influences become significant as the system approaches the static regime. In the static regime, small values of Re_{db} have minimal effect on the phase boundary potential, but for the highest Re_{db} values examined we observe instances where the potential is than three times its expected value in the absence of flow (denoted via horizontal lines in Figure 5).

The change in the phase boundary potential with Re_{db} is highly dependent upon the values of ψ_f and Sc as is evident in Figure 6, where we plot the potential in the static limit. Specifically, results apply when $tD/\lambda_{db}^2 = 10$. For

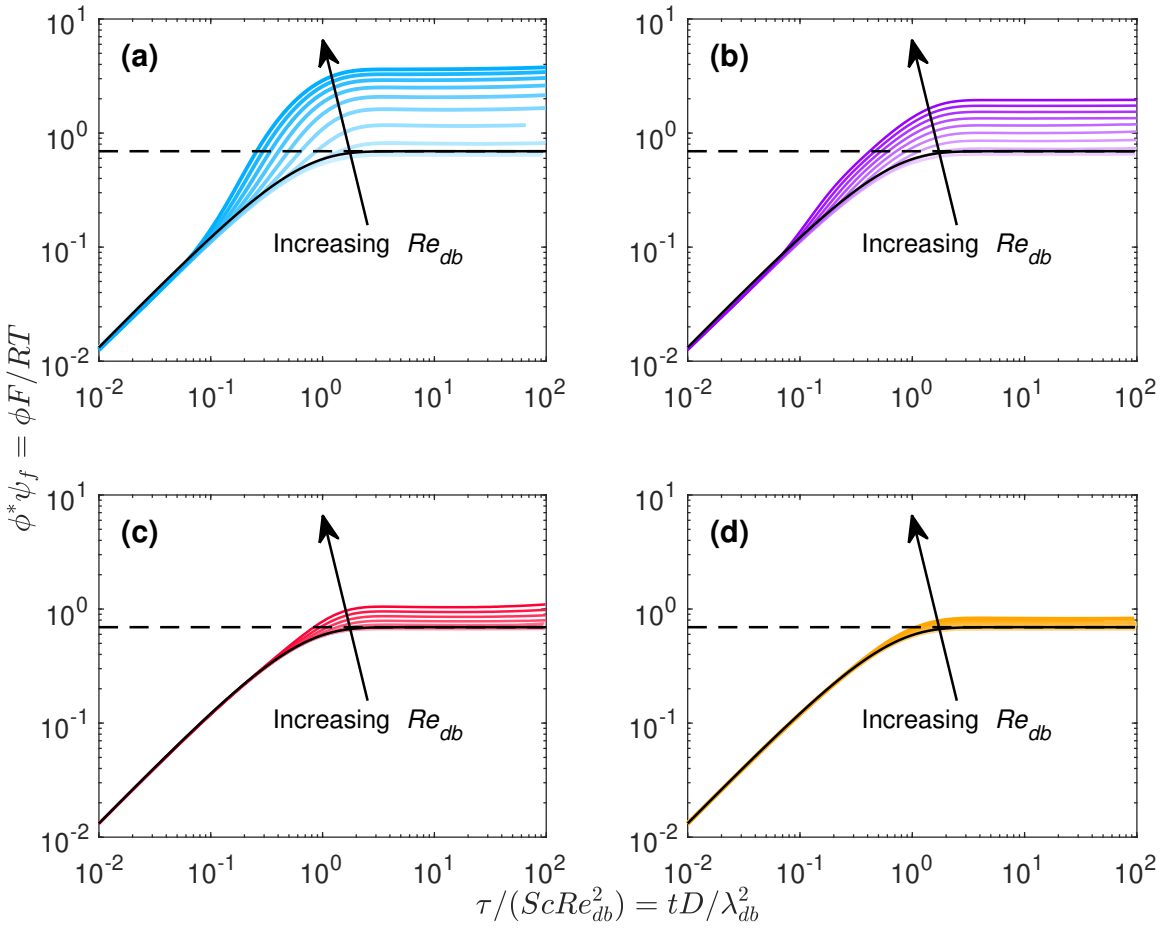

Fig. 5 Dimensionless potential temporal evolution with varying Re_{db} (Range of 0.1 to 1 in increments of 0.1 indicated by varying color saturation) with (a) $\psi_f = 1$ and $Sc = 1000$ (b) $\psi_f = 1$ and $Sc = 100$ (c) $\psi_f = 0.1$ and $Sc = 1000$ (d) $\psi_f = 0.1$ and $Sc = 100$. Results are plotted along side the potential predicted by Equation 3 (dashed black line) and the no-flow case, $Re_{db} = 0$, from Figure 2 (solid black line).

the case of $\psi_f = 0.1$ and $Sc = 100$, the effect of Re_{db} on the static potential is minimal, with the potential increasing from a value of 0.69 at $Re_{db} = 0.1$ to a value of 0.83 at $Re_{db} = 1$. For the case of $\psi_f = 1$ and $Sc = 1000$, the effect of Re_{db} on the static potential is more substantial, with the potential increasing to a value of 3.6 at $Re_{db} = 1$. Both Sc and Re_{db} parameterize the extent with which external flow affects the diffuse ionic double layers near the membrane-water interface; higher Sc diminishes ion diffusion in comparison to flow, while higher Re_{db} diminishes space charge induced potential effects. ψ_f, the ratio of the fluid kinetic energy to system characteristic electrostatic energy, serves as an amplification factor, increasing the extent that flow-ion interaction has on the phase boundary potential. To more clearly discern fluid flow effects and better define the influence of each dimensionless ratio, we introduce the enhancement coefficient η, which compares the static portion of the potential ($\frac{\tau}{ScRe_{db}^2} >> 1$) to the expected potential in the case of no-flow from Equation 3:

$$\eta = \frac{2\phi^*\psi_f}{ln\frac{K_+}{K_i}} - 1; \tag{4}$$

An η of zero indicates no change in phase boundary potential from its zero-flow limit. The enhancement coefficient may be modeled as a function of the previously defined system parameters, namely Re_{db}, ψ_f and Sc, alongside dimensionless numbers parameterizing system length ratios and the properties of the fluid, membrane, and ions. We attempted to develop this function through two methods. First, following a trial-and-error route, we anticipate that the correlation for the enhancement coefficient will be functionally similar to heat and mass transfer coefficients, i.e., in the form of $\eta = \psi_f^{\alpha} f(Re_{db}^{\beta} Sc^{\gamma})$, where f is some function of $Re_{db}^{\beta} Sc^{\gamma}$ and α, β and γ are unknown fitting parameters. Fitting $\alpha = \frac{2}{5}$, $\beta = \frac{4}{5}$ and $\gamma = \frac{1}{3}$, we plot all results obtained in this study in Figure 7 with the ratio of η/ψ_f^{α} on the y-axis and $Re_{db}^{\beta} Sc^{\gamma}$ on x-axis. Plotted results are also provided in a table in the supporting information. To further determine the functional dependence of η on Re_{db} and Sc, we define the fluid scaling parameter $\omega_1 = Re_{db}^{\beta} Sc^{\gamma}$. When ω_1 is small, the transport of ions is dominated by diffusion having little influence from the fluid flow. Conversely, when ω_1 is large, ion transport is dominated by convective effects. Plotting $\eta\psi_f^{-\alpha}$ as a function of ω_1 in Figure 7, we find excellent collapse for all simulated conditions. We subsequently fit the collapsed result using the ratio of two power series in the form of $\eta\psi_f^{-2/5} = \frac{\sum_{i=0}^{N} a_i \omega_1^i}{\sum_{j=0}^{N-l} a_j \omega_1^j}$ where a_i are unknown coefficients and l determines the fitting behavior when $\omega \to \infty$; for example when $l = 1$, the fit equation reduces to a first order polynomial with a slope of $\frac{a^N}{a^{N-1}}$. We elect to use a value of $N = 4$ and $l = 1$ resulting in the following function

$$\eta = \psi_f^{2/5} \frac{a_1\omega_1^2 + a_2\omega_1^3 + a_3 a_4 \omega_1^4}{1 + a_5\omega_1 + a_6\omega_1^2 + a_4\omega_1^3} \tag{5}$$

where $a_1 = 1.92 \cdot 10^{-2}$, $a_2 = -1.47 \cdot 10^{-2}$, $a_3 = 0.68$, $a_4 = 4.3 \cdot 10^{-3}$, $a_5 = -0.212$ and $a_6 = 7.06 \cdot 10^{-3}$. Coefficients were obtained by the Curve Fitting Toolbox in MATLAB [48], and were selected because all values of $\omega_1 > 0$ produce a strictly positive enhancement $\eta > 0$, and they by definition lead to $\omega_1 \to 0$ as $\eta \to 0$ and also to $\eta \propto 0.68\omega_1\psi_f^{2/5}$ as $\omega_1 \to \infty$. Examining the data in Figure 7, we see a transition near $\omega_1 = 3$ where the effective enhancement ($\eta\psi^{-2/5}$) departs from a value near 0 to a near-linear scaling of 0.7 in the range of $5 < \omega_1 < 10$. Although some values of η are negative at small ω_1, we believe these to be caused by small numerical errors, and since their relative magnitude is close to 0, will treat such values as effectively zero. The existence of a transition between no enhancement ($\omega_1 < 3$) and linear scaling ($\omega_1 > 3$) suggests that there is a critical degree of ion advection, as characterized by ω_1, that must occur before the effect of external flow is to increase the phase boundary potential.

Membrane based ion-selective electrodes tend to have lower detection limits in the range of $1 \cdot 10^{-7}$ to $1 \cdot 10^{-6}$ M [49]. To put the above analysis of ω_1 into context we estimate that an external flow velocity of at least 16 cm s^{-1} is needed for $\omega_1 > 3$, assuming a $1 \cdot 10^{-7}$ M solution at room temperature (300K) and an ion diffusion coefficient of $1 \cdot 10^{-9}$ m^2 s^{-1}. This fluid velocity is well above the velocities encountered for such sensors in the majority of applications, which suggests that changes in phase boundary potential from external flow will only occur for very dilute systems and in the absence of a background electrolyte. The effects of varying single ion partition coefficients, variable

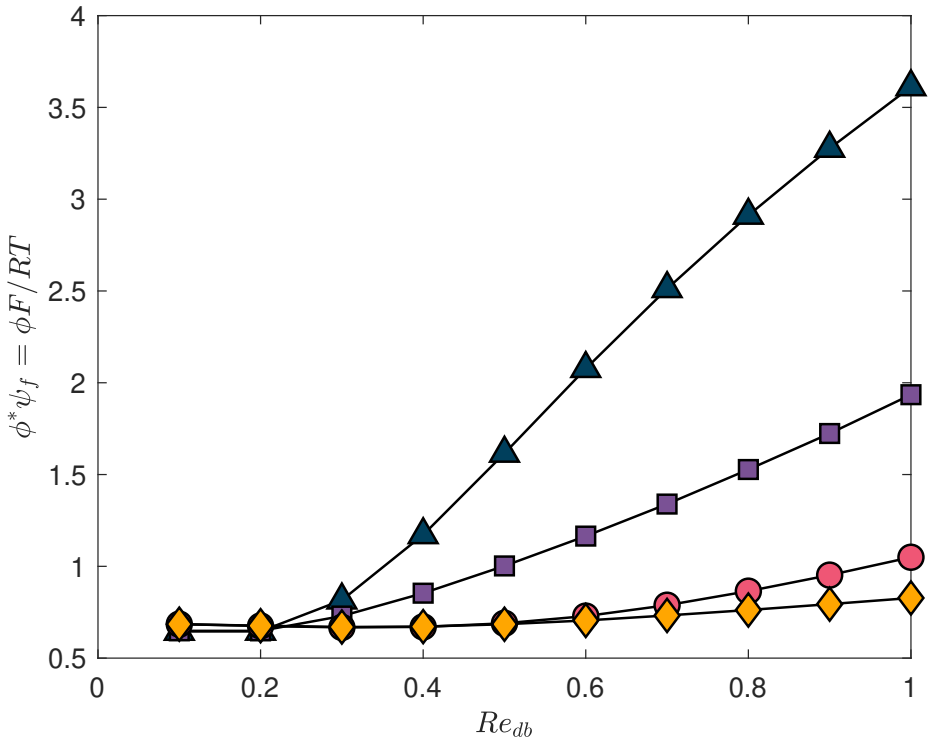

Fig. 6 Values at $\frac{\tau}{ScRe_{db}^2} = 10$ plotted for $\psi_f = 1$ and $Sc = 1000$ (blue triangle), $\psi_f = 1$ and $Sc = 100$ (purple square), $\psi_f = 0.1$ and $Sc = 1000$ (red circle) and $\psi_f = 0.1$ and $Sc = 100$ (orange diamond)

ion diffusion coefficients and variable ion concentrations in solution was not explored in this study, which may affect the exact limit at which external flow (ω_1) affects the phase boundary potential. Regardless, our results indicate that effects of external flow on membrane systems are more pronounced in the low concentration limit. This result is consistent with previous studies on reversed electrolysis cells were the greatest effect of flow on ion transport occurred for the smallest ion concentrations [9].

As a second approach to collapse results, we note that results do apply for the membrane which is of a specific length $L_m^* = 20.0$ (non-dimensionalized by $\frac{\nu}{U_0}$). To examine the interplay between different length scales affecting the problem, we define a dimensionless ratio $\omega_2 = \frac{\lambda_{db}}{\delta_m}$, where δ_m is a characteristic mass transfer layer thickness for the fluid after traveling a distance L_m (dimensional) along the membrane. δ_m can be defined as $\delta_m = \left(\frac{DL_m}{\lambda_{db}\gamma_s}\right)^{1/2}$, where γ_s is the characteristic shear rate. The shear rate, in turn, scales as $\gamma_s = \frac{U_0}{\delta_{mom}}$, with $\delta_{mom} = \left(\frac{L_m \nu}{U_0}\right)^{1/2}$. Combining these definitions yields:

$$\omega_2 = \frac{\lambda_{db}^{3/2} U_0^{3/4}}{D^{1/2} L_m^{3/4} \nu^{1/4}} \frac{\nu^{1/2}}{\nu^{1/2}} = Sc^{1/2} Re_{db}^{3/4} \left(\frac{\lambda_{db}}{L_m}\right)^{3/4} \tag{6}$$

Equation 6 leads to a similar functional form for ω_2 as empirically found for ω_1, but with an added term of $\frac{\lambda_{db}}{L_m}$ raised to the $3/4$ power. We plot $\eta\psi^{-2/5}$ versus ω_2 in Figure 8 for all test case performed here along side a line of best fit in the form of Equation 5. We retain the scaling of $\psi^{-2/5}$ as this find close to optimum in fitting. While the collapse of results

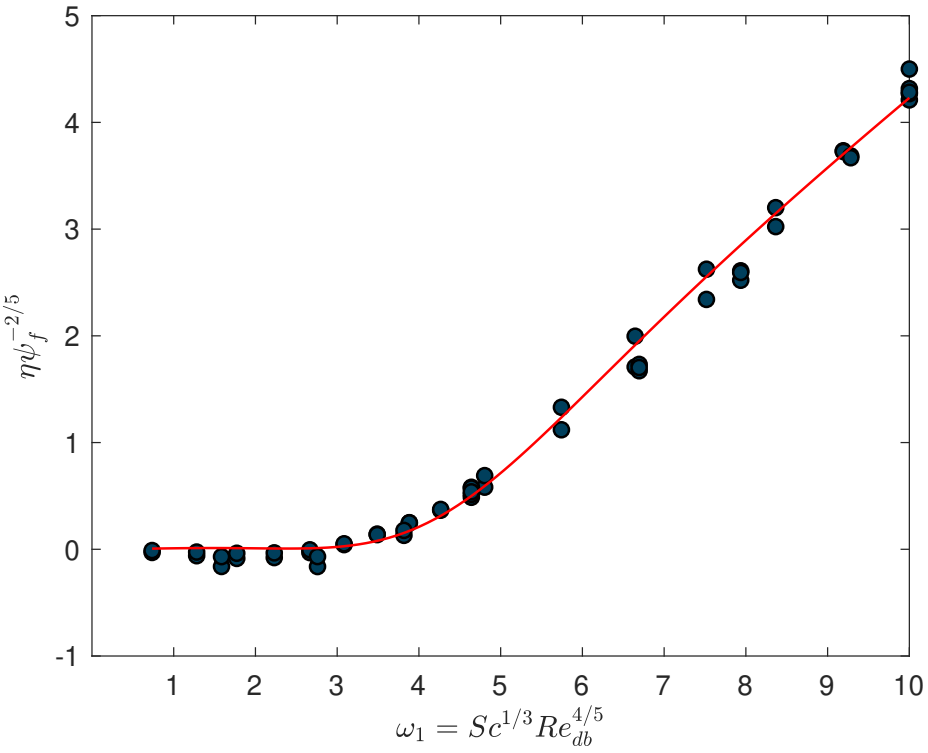

Fig. 7 Potential enhancement factor η scaled by $\psi_f^{-2/5}$ and plotted as a function of system Schmidt number (Sc) and Debye length Reynolds number (Re_{db}) for all data (blue circles). Data fitting is provided by Equation 5 and is shown as the red solid line.

is not as strong as the empirically-tuned result with ω_1, examination of ω_2 supports the scaling $\eta = \psi_f^{\alpha} f(Re_{db}^{\beta} Sc^{\gamma})$, and further suggests how results may be affected by adjusting the membrane length. Results would additionally be influenced by changes in ion partition coefficients for cationic and anionic species, as well as by utilizing unequal diffusion coefficients for species or unequal electrical permittivities for the fluid and membrane. For this reason, the solutions presented here cannot be considered universal, with additional simulations required to capture the influences of changing geometry,changing ion properties, and changing fluid and membrane electrical properties.

IV. Conclusion

We developed a code by modifying the open source library OpenFOAM to solve the Navier-Stokes-Nernst-Planck-Poisson set of equations to examine coupled mass transfer, fluid flow, and electrostatic potentials for non-equal partitioning ions at membrane-water interface. This code was used specifically to explore the effects of external viscous flow on the diffuse ionic double layers at the interface of an ISE membrane and aqueous sample and associated changes in phase boundary potential. Framing the problem in a manner similar to mass transfer in a developing boundary layer and utilizing an associated dimensionless framework revealed that the dimensionless numbers $\omega_1 = Re_{db}^{4/5} Sc^{1/3}$ or $\omega_2 = Re_{db}^{3/4} Sc^{1/2} \left(\frac{\lambda_{db}}{L_m}\right)^{3/4}$, which are functions of the Debye-length Reynolds Number and the Schmidt number, not

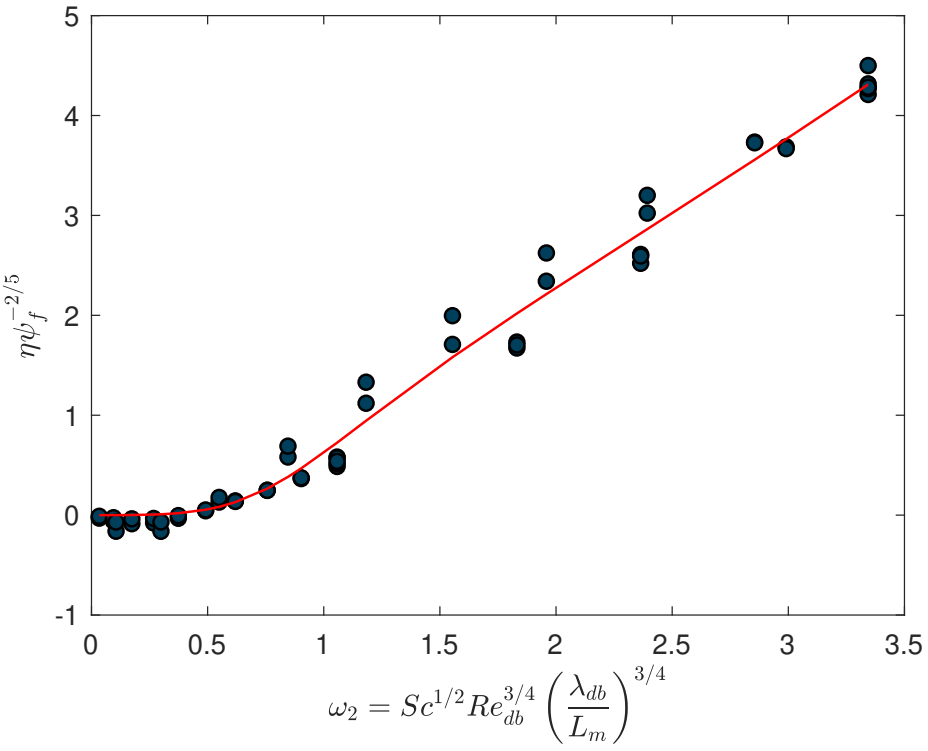

Fig. 8 Potential enhancement factor η scaled by $\psi_f^{-2/5}$ and plotted as a function of system Schmidt number (Sc) and Debye length Reynolds number (Re_{db}) for all data (blue circles) using the fluid scaling parameter ω_2 as defined in Equation 6. The red solid line represents data fitting by Equation 5 with coefficients $a_1 = 6.14 \cdot 10^{-3}$, $a_2 = 9.80 \cdot 10^{-2}$, $a_3 = 2.12$, $a_4 = 1.76 \cdot 10^{-1}$, $a_5 = -1.11$ and $a_6 = 6.98 \cdot 10^{-1}$.

only are appropriate metrics (switches) to determine if hydrodynamic forces affect the formation of the diffuse ionic double layers, but also can be used to quantitatively predict the extent to which fluid flow affects the phase boundary potential. Although this study focused on a sole geometry and set of partition concentrations, the results show the applicability of traditional heat and mass transfer analysis to describe ion transport at ISE membrane and aqueous sample interfaces in electrohydrodynamic flows, as it is relevant to ISEs and other system where phase boundary potential modeling is of interest.

V. Supplemental

A link to the Github repository for the code, implementation details for the time step controller, additional code validation cases, and tabulated data plotted in Figure 7 are available online.

VI. CRediT authorship contribution statement

A.J. Andrews: Conceptualization, Software, Formal analysis, Investigation, Methodology, Data curation, Writing - original draft, Writing - review & editing. P. Bühlmann: Conceptualization, Funding acquisition, Investigation, Writing - review & editing. C.J. Hogan: Conceptualization, Investigation, Methodology, Supervision, Writing - original draft,

Writing - review & editing.

VII. Acknowledgments

The authors acknowledge the Minnesota Supercomputing Institute (MSI) at the University of Minnesota for providing resources that contributed to the research results reported within this paper. P.B. acknowledges support by National Science Foundation Grant CHE-1748148 and CHE-2203752.

References

[1] Flagan, R. C., "History of Electrical Aerosol Measurements," *Aerosol Science and Technology*, Vol. 28, No. 4, 1998, pp. 301–380. https://doi.org/10.1080/02786829808965530.

[2] Mizuno, A., "Electrostatic precipitation," *IEEE Transactions on Dielectrics and Electrical Insulation*, Vol. 7, No. 5, 2000, pp. 615–624. https://doi.org/10.1109/94.879357.

[3] Wang, W., Luo, Q., Li, B., Wei, X., Li, L., and Yang, Z., "Recent Progress in Redox Flow Battery Research and Development," *Advanced Functional Materials*, Vol. 23, No. 8, 2013, pp. 970–986. https://doi.org/10.1002/adfm.201200694.

[4] Werber, J. R., Osuji, C. O., and Elimelech, M., "Materials for next-generation desalination and water purification membranes," *Nature Reviews Materials*, Vol. 1, 2016. https://doi.org/10.1038/natrevmats.2016.18.

[5] Bobacka, J., Ivaska, A., and Lewenstam, A., "Potentiometric Ion Sensors," *Chemical Reviews*, Vol. 108, No. 2, 2008, pp. 329–351. https://doi.org/10.1021/cr068100w.

[6] Bakker, E., Bühlmann, P., and Pretsch, E., "Polymer Membrane Ion-Selective Electrodes–What are the Limits?" *Electroanalysis*, Vol. 11, No. 13, 1999, pp. 915–933. https://doi.org/10.1002/(SICI)1521-4109(199909)11:13<915::AID-ELAN915>3.0.CO;2-J.

[7] Bakker, E., Bühlmann, P., and Pretsch, E., "The phase-boundary potential model," *Talanta*, Vol. 63, No. 1, 2004, pp. 3–20. https://doi.org/10.1016/j.talanta.2003.10.006.

[8] Sokalski, T., Ceresa, A., Zwickl, T., and Pretsch, E., "Large Improvement of the Lower Detection Limit of Ion-Selective Polymer Membrane Electrodes," *Journal of the American Chemical Society*, Vol. 119, No. 46, 1997, pp. 11347–11348. https://doi.org/10.1021/ja972932h.

[9] Długołęcki, P., Anet, B., Metz, S. J., Nijmeijer, K., and Wessling, M., "Transport limitations in ion exchange membranes at low salt concentrations," *Journal of Membrane Science*, Vol. 346, No. 1, 2010, pp. 163–171. https://doi.org/10.1016/j.memsci.2009.09.033.

[10] Eisenman, G., Sandblom, J. P., and Walker, J. L., "Membrane Structure and Ion Permeation," *Science*, Vol. 155, No. 3765, 1967, pp. 965–974. https://doi.org/10.1126/science.155.3765.965.

[11] Zhurov, K., Dickinson, E. J., and Compton, R. G., "Dynamics of ion transfer potentials at liquid-liquid interfaces," *Journal of Physical Chemistry B*, Vol. 115, 2011, pp. 6909–6921. https://doi.org/10.1021/jp202318y.

[12] Jasielec, J. J., Sokalski, T., Filipek, R., and Lewenstam, A., "Neutral-Carrier Ion-Selective Electrodes Assessed by the Nernst–Planck–Poisson Model," *Analytical Chemistry*, Vol. 87, No. 17, 2015, pp. 8665–8672. https://doi.org/10.1021/acs.analchem.5b00065.

[13] Jasielec, J. J., Mousavi, Z., Granholm, K., Sokalski, T., and Lewenstam, A., "Sensitivity and Selectivity of Ion-Selective Electrodes Interpreted Using the Nernst-Planck-Poisson Model," *Analytical Chemistry*, Vol. 90, No. 15, 2018, pp. 9644–9649. https://doi.org/10.1021/acs.analchem.8b02659.

[14] Flavin, M. T., Freeman, D. K., and Han, J., "Interfacial ion transfer and current limiting in neutral-carrier ion-selective membranes: A detailed numerical model," *Journal of Membrane Science*, Vol. 572, 2019, pp. 374–381. https://doi.org/10.1016/j.memsci.2018.10.065.

[15] Brumleve, T. R., and Buck, R. P., "Numerical solution of the Nernst-Planck and poisson equation system with applications to membrane electrochemistry and solid state physics," *Journal of Electroanalytical Chemistry and Interfacial Electrochemistry*, Vol. 90, No. 1, 1978, pp. 1–31. https://doi.org/10.1016/S0022-0728(78)80137-5.

[16] Chang, H., and Jaffé, G., "Polarization in Electrolytic Solutions. Part I. Theory," *The Journal of Chemical Physics*, Vol. 20, No. 7, 1952, pp. 1071–1077. https://doi.org/10.1063/1.1700669.

[17] Nikonenko, V. V., Kovalenko, A. V., Urtenov, M. K., Pismenskaya, N. D., Han, J., Sistat, P., and Pourcelly, G., "Desalination at overlimiting currents: State-of-the-art and perspectives," *Desalination*, Vol. 342, 2014, pp. 85–106. https://doi.org/https://doi.org/10.1016/j.desal.2014.01.008.

[18] Uzdenova, A., and Urtenov, M., "Potentiodynamic and Galvanodynamic Regimes of Mass Transfer in Flow-Through Electrodialysis Membrane Systems: Numerical Simulation of Electroconvection and Current-Voltage Curve," *Membranes*, Vol. 10, No. 3, 2020. https://doi.org/10.3390/membranes10030049.

[19] Li, G., Townsend, A., Archer, L. A., and Koch, D. L., "Electroconvection near an ion-selective surface with Butler–Volmer kinetics," *Journal of Fluid Mechanics*, Vol. 930, 2022, p. A26. https://doi.org/10.1017/jfm.2021.907.

[20] Kwak, R., Pham, V. S., and Han, J., "Sheltering the perturbed vortical layer of electroconvection under shear flow," *Journal of Fluid Mechanics*, Vol. 813, 2017, p. 799–823. https://doi.org/10.1017/jfm.2016.870.

[21] Kwak, R., Pham, V. S., Lim, K. M., and Han, J., "Shear Flow of an Electrically Charged Fluid by Ion Concentration Polarization: Scaling Laws for Electroconvective Vortices," *Phys. Rev. Lett.*, Vol. 110, 2013, p. 114501. https://doi.org/10.1103/PhysRevLett.110.114501.

[22] Li, G., Townsend, A., Archer, L. A., and Koch, D. L., "Suppression of electroconvective and morphological instabilities by an imposed cross flow of the electrolyte," *Phys. Rev. Fluids*, Vol. 6, 2021, p. 033701. https://doi.org/10.1103/PhysRevFluids.6.033701.

[23] Nikonenko, V. V., Mareev, S. A., Pis'menskaya, N. D., Uzdenova, A. M., Kovalenko, A. V., Urtenov, M. K., and Pourcelly, G., "Effect of electroconvection and its use in intensifying the mass transfer in electrodialysis (Review)," *Russian Journal of Electrochemistry*, Vol. 53, No. 10, 2017, pp. 1122–1144. https://doi.org/10.1134/S1023193517090099.

[24] Mitscha-Baude, G., Buttinger-Kreuzhuber, A., Tulzer, G., and Heitzinger, C., "Adaptive and iterative methods for simulations of nanopores with the PNP–Stokes equations," *Journal of Computational Physics*, Vol. 338, 2017, pp. 452–476. https://doi.org/10.1016/j.jcp.2017.02.072.

[25] Park, J.-W., Kim, C., Park, J., and Hwang, J., "Computational Fluid Dynamic Modelling of Particle Charging and Collection in a Wire-to-Plate Type Single-Stage Electrostatic Precipitator," *Aerosol and Air Quality Research*, Vol. 18, No. 3, 2018, pp. 590–601. https://doi.org/10.4209/aaqr.2017.05.0176.

[26] Lastow, O., and Balachandran, W., "Numerical simulation of electrohydrodynamic (EHD) atomization," *Journal of Electrostatics*, Vol. 64, No. 12, 2006, pp. 850–859. https://doi.org/10.1016/j.elstat.2006.02.006.

[27] He, M., and Sun, P., "Mixed finite element analysis for the Poisson–Nernst–Planck/Stokes coupling," *Journal of Computational and Applied Mathematics*, Vol. 341, 2018, pp. 61–79. https://doi.org/10.1016/j.cam.2018.04.003.

[28] Issa, R., "Solution of the implicitly discretised fluid flow equations by operator-splitting," *Journal of Computational Physics*, Vol. 62, No. 1, 1986, pp. 40–65. https://doi.org/10.1016/0021-9991(86)90099-9.

[29] Hagelaar, G., and Kroesen, G., "Speeding Up Fluid Models for Gas Discharges by Implicit Treatment of the Electron Energy Source Term," *Journal of Computational Physics*, Vol. 159, No. 1, 2000, pp. 1–12. https://doi.org/10.1006/jcph.2000.6445.

[30] Weller, H. G., Tabor, G., Jasak, H., and Fureby, C., "A tensorial approach to computational continuum mechanics using object-oriented techniques," *Computers in Physics*, Vol. 12, No. 6, 1998, pp. 620–631. https://doi.org/10.1063/1.168744.

[31] Holzmann, T., *Mathematics, Numerics, Derivations and OpenFOAM(R)*, Holzmann CFD, 2019. https://doi.org/10.13140/RG.2.2.27193.36960.

[32] Cramer, K. R., and Pai, S. I., *Magnetofluid dynamics for engineers and applied physicists*, McGraw-Hill Book Company, 1973.

[33] Haroun, Y., Legendre, D., and Raynal, L., "Volume of fluid method for interfacial reactive mass transfer: Application to stable liquid film," *Chemical Engineering Science*, Vol. 65, No. 10, 2010, pp. 2896–2909. https://doi.org/https://doi.org/10.1016/j.ces.2010.01.012.

[34] Haroun, Y., Legendre, D., and Raynal, L., "Direct numerical simulation of reactive absorption in gas–liquid flow on structured packing using interface capturing method," *Chemical Engineering Science*, Vol. 65, No. 1, 2010, pp. 351–356. https://doi.org/10.1016/j.ces.2009.07.018.

[35] Bouras, H., Haroun, Y., Philippe, R., Augier, F., and Fongarland, P., "CFD modeling of mass transfer in Gas-Liquid-Solid catalytic reactors," *Chemical Engineering Science*, Vol. 233, 2021, p. 116378. https://doi.org/10.1016/j.ces.2020.116378.

[36] Greenshields, C., and Weller, H., *Notes on Computational Fluid Dynamics: General Principles*, CFD Direct Ltd, Reading, UK, 2022.

[37] Alexander, R., "Diagonally Implicit Runge-Kutta Methods for Stiff O.D.E.'s," *SIAM Journal on Numerical Analysis*, Vol. 14, No. 6, 1977, pp. 1006–1021. https://doi.org/10.1137/0714068.

[38] Kennedy, C. A., and Carpenter, M. H., "Diagonally Implicit Runge-Kutta Methods for Ordinary Differential Equations. A Review," , 2016. URL http://www.sti.nasa.gov.

[39] Jasak, H., "Error Analysis and Estimation for the finite volume method with applications to fluid flows." Ph.D. thesis, Imperial College London, 1996.

[40] D'Alessandro, V., Binci, L., Montelpare, S., and Ricci, R., "On the development of OpenFOAM solvers based on explicit and implicit high-order Runge–Kutta schemes for incompressible flows with heat transfer," *Computer Physics Communications*, Vol. 222, 2018, pp. 14–30. https://doi.org/10.1016/j.cpc.2017.09.009.

[41] Yoon, M., Yoon, G., and Min, C., "On Solving the Singular System Arisen from Poisson Equation with Neumann Boundary Condition," *Journal of Scientific Computing*, Vol. 69, No. 1, 2016, pp. 391–405. https://doi.org/10.1007/s10915-016-0200-2.

[42] Paulo J. Oliveira, R. I. I., "An Improved PISO Algorithm for the Computation of Buoyancy-Driven Flows," *Numerical Heat Transfer, Part B: Fundamentals*, Vol. 40, No. 6, 2001, pp. 473–493. https://doi.org/10.1080/104077901753306601.

[43] Leonard, G. L., Mitchner, M., and Self, S. A., "An experimental study of the electrohydrodynamic flow in electrostatic precipitators," *Journal of Fluid Mechanics*, Vol. 127, 1983, p. 123–140. https://doi.org/10.1017/S0022112083002657.

[44] Schönke, J., "Unsteady analytical solutions to the Poisson–Nernst–Planck equations," *Journal of Physics A: Mathematical and Theoretical*, Vol. 45, No. 45, 2012, p. 455204. https://doi.org/10.1088/1751-8113/45/45/455204.

[45] Schlichting, H., and Gersten, K., *Boundary-Layer Theory*, Springer, Berlin, Heidelberg, 2017. https://doi.org/10.1007/978-3-662-52919-5.

[46] Quoc Hung, L., "Electrochemical properties of the interface between two immiscible electrolyte solutions: Part I. Equilibrium situation and galvani potential difference," *Journal of Electroanalytical Chemistry and Interfacial Electrochemistry*, Vol. 115, No. 2, 1980, pp. 159–174. https://doi.org/https://doi.org/10.1016/S0022-0728(80)80323-8.

[47] Ward, K. R., Dickinson, E. J. F., and Compton, R. G., "Dynamic Theory of Membrane Potentials," *The Journal of Physical Chemistry B*, Vol. 114, No. 33, 2010, pp. 10763–10773. https://doi.org/10.1021/jp102599j.

[48] The MathWorks, I., *Curve Fitting Toolbox*, Natick, Massachusetts, United State, 2020. URL https://www.mathworks.com/products/curvefitting.html.

[49] Bakker, E., Bühlmann, P., and Pretsch, E., "Carrier-Based Ion-Selective Electrodes and Bulk Optodes. 1. General Characteristics," *Chemical Reviews*, Vol. 97, No. 8, 1997, pp. 3083–3132. https://doi.org/10.1021/cr940394a.

Determination of Forced Convection Effects on the Response of Membrane-Based Ion-Selective Electrodes via Numerical Solution to the Navier-Stokes-Nernst-Plank-Poisson Equations

Austin J. Andrews*,Philippe Bühlmann † and Christopher J. Hogan ‡

Ion selective electrodes (ISEs) enable measurements via the build-up of a phase boundary potential at the surface of a sensing membrane. While a framework exists to understand the performance of ISEs in stagnant samples, the influences of fluid flow on ISEs is less studied. We model the transport of charged ions in solution occurring near interfaces between ISE membranes and aqueous samples when subject to an external flow. We developed a numerical model extending the Pressure-Implicit with Splitting of Operators (PISO) algorithm to incorporate the Navier-Stokes-Nernst-Plank-Poisson system of equations. We find that external flow distorts the aqueous side of the formed double layer at the ISE membrane and aqueous sample interface, leading to an increase in the phase boundary potential. The change in potential is shown to be a function of a novel set of dimensionless numbers, most notably the Debye Length Reynolds number, i.e., the Reynolds number with the Debye Length as the system dimension.

I. Introduction

The transport of dilute, charged species via both hydrodynamic and electrostatic forces governs a variety of engineered systems, including but not limited to charged particle transport in aerosols[1] and their collection in electrostatic precipitators [2], flow batteries [3], desalination processes [4], and ion-selective electrodes (ISEs) [5]. In many of these instances, in particular the latter, charged species transport is not only affected by external and internal electric fields, but also through the unequal partitioning of charged species (solutes) at phase boundaries. Unequal partitioning leads to charge separation at the interface and formation of an electric double layer; this ultimately leads to a measurable potential difference. For ISEs, the potential difference arises at the interface of the ISE membrane and an aqueous solution that contains the analyte ion of interest. Formation of this phase boundary potential allows for the measurement of the concentration of this analyte ion. Considerable effort has been dedicated to the design of specific membrane materials to obtain selectivity for various different target ions [6]. In general, ISE membranes comprise (i) a polymeric membrane matrix that provides the membrane with mechanical robustness, (ii) the analyte ion either

*Graduate Research Assistant, University of Minnesota, 111 Church St SE, Minneapolis, MN 55455
†Professor, University of Minnesota, 207 Pleasant St SE, Minneapolis, MN 55455
‡Professor, University of Minnesota, 111 Church St SE, Minneapolis, MN 55455

in a free form or in the form of a complex with an ion-selective receptor (usually referred to as ionophore), as well as a (iii) counter ion (referred to as ionic site) that is either covalently attached to the matrix polymer or has such a high hydrophobicity that leaching into aqueous samples is negligible. A phase boundary potential forms because the analyte ion and counterions differ in their free energies of transfer from the sample into the membrane phase [7]. While ISE theory typically assumes local equilibrium at the interface of the sample and membrane phase, the transport of ions between the two phases both by diffusion and convection may influence the magnitude of the phase boundary potential. A well-known illustration for this are the zero-current transmembrane ion fluxes that often determine the lower detection limits of ISEs [8]. Also, through experimental measurements of membrane resistance, Dlugolecki et al. found that external fluid flow may influence the electric double layer particularly for low solution concentrations [9]. However, the effect of fluid flow on phase boundary potentials has only been qualitatively explored in prior work, mainly because explicit computation of ion transport accounting for fluid flow requires numerical solution to the Navier-Stokes-Nernst-Plank-Poisson (NS-NPP) set of equations, which combine conservation of mass and momentum for fluid flow with mass conservation of each charged species, with Poisson's equation for the electric potential. This is a complex set of equations with extensive coupling, and is a stiff system of equations.

Modeling of ISEs presents unique challenges due to the need to account for ion exchange at the ISE membrane and aqueous sample interface. Ions differentially transport across membrane interfaces primarily due to differences in affinity for the sample and the membrane phase and may be further altered by binding of the analyte ion to ion receptors in the membrane phase [10]. Prior work conducted for modeling ISE systems has hence more frequently examined numerical solutions to the NPP equations, i.e. the Nernst-Planck-Poisson (NPP) equations, which do not consider fluid flow [11–15]. In these studies, there has been two primarily employed methods to handle the phase boundary interface. First, coupling between phases has been accomplished using two separate simulation domains, with the Chang-Jaffe boundary condition [13, 16] at the interface, which relates the flux across the ISE membrane and aqueous sample interface to a reversible 1st order reaction. Second, interface mass transfer has been modeled by generalizing ion transport to include gradients in ion activity [14], allowing for a singular domain, keeping track of spatial variations in the affinity of ions for the two contacting phases.

There have been studies exploring the effects of fluid flow on ion motion within flow-through ion exchange membranes that are used for electrodialysis (ED)[17–22]. In these studies, the NS-NPP equations were applied, but their their use was limited to the aqueous phase, focusing on electroconvection and instabilities occurring from an applied external voltage. The ion concentrations at the phase boundaries were determined by boundary conditions such as specifying a fixed ion concentration[18] or modeling by Butler-Volmer kinetics[19]. In contrast to electrodialysis systems, ISE sensing devices are rarely operated with an applied external potential and hence ion currents in ISEs are usually near zero. Instabilities that lead to electroconvection generally occur when the ion currents are beyond the ohmic region [23]. Therefore, it is expected that fluid instabilities arising in ED cells are absent from the problems considered

in this study, where no external potential is applied.

As understanding the potential response is critical to the design and implementation of ISEs as sensing devices, it is important to know if and when external flow affects the response of such devices, and to probe fundamental behavior of systems with coupled ion mass transfer, fluid flow, and electrostatics at interfaces. In addition to applications in electrodialysis, the NS-NPP equations have been solved to predict the behavior of nanopore sensors [24], model electrostatic precipitators [25], and examine EHD-assisted droplet formation (i.e. electrosprays) [26], among others. As alluded to above, numerical solutions of these sets of equations has been particularly difficult, and the choice of numerical schemes is crucial to ensure accuracy and convergence [27]. As the aforementioned works utilize different numerical schemes, we believe there is still a need to advance NS-NPP solution schemes and to examine fundamental NS-NPP transport solutions near phase boundaries. Towards this end, here we develop an NS-NPP solution scheme to model ion transport and the evolution of the phase boundary potential in systems that approximate ISEs and which also resemble classical laminar flow boundary layers. Described in the subsequent section, the numerical solution scheme developed utilizes the finite volume method for spatial discretization and extends Issa's Pressure-Implicit with Splitting of Operators (PISO) [28] solution algorithm for incompressible flows to include coupling between the NS and NPP equations. The NPP equations are solved using Hagelaar's method [29]. A high order embedded Runge-Kutta(RK) method with variable step size is used for time discretization. Development of this method was conducted using the open source package OpenFOAM [30]. Algorithm validation is performed via comparison to a series of analytical solutions, classical solutions, and prior experiments. Subsequently, the algorithm is applied to examine the phase boundary potential developed across a membrane while simultaneously a laminar boundary layer develops (i.e., the Blasius solution augmented by mass transfer of charged species). We show that the dimensionless phase boundary potential is positively correlated to increased fluid flow and decreased ion diffusion rates.

II. Theory and Solution Scheme

A. Governing Equations

To model the effects of fluid flow on ion transport in ISE systems, with the assumptions of incompressible (assuming low fluid Mach number), laminar (low fluid Reynolds number) and isothermal flow, the Navier-Stokes equations (Equation 1a and Equation 1n), Nernst-Planck equation (Equation 1d), and Poisson equation (Equation 1c) are employed

and are defined as:

$$\nabla \cdot \vec{U} = 0 \tag{1a}$$

$$\frac{\partial \vec{U}}{\partial t} + \vec{U}\nabla \cdot \vec{U} = -\nabla \frac{P}{\rho_f} + \nu \nabla^2 \vec{U} + \nabla \cdot \nu[(\nabla \vec{U})^T - \frac{2}{3}(\nabla \vec{U})] + \frac{f_e}{\rho_f} \tag{1b}$$

$$\nabla \cdot \epsilon \nabla \phi = \sum_{i=1}^{i=n} F c_i z_i \nabla \phi \tag{1c}$$

$$\frac{\partial c_i}{\partial t} + \nabla \cdot (c_i[\vec{U} + z_i \frac{F D_i}{RT} \nabla \phi + \Theta]) = \nabla \cdot D_i \nabla c_i \tag{1d}$$

$$\Theta = \frac{D_i(1 - k_i)}{\alpha + k_i(1 - \alpha)} \nabla \alpha \tag{1e}$$

where $\vec{U}$ is the fluid velocity, P is the hydrodynamic pressure, ρ_f is the fluid density, ν is the fluid kinematic viscosity, ϕ is the electrostatic potential, f_e is the electrostatic body force, ϵ is the permittivity, F the Faraday constant, c_i the molar concentration of ion species i, z_i the charge of species i, D_i the ion diffusion coefficient, R the universal gas constant, T the temperature of the surrounding medium, k_i is the single ion partition coefficients, and α the membrane mass fraction, differentiating between the membrane phase ($\alpha = 1$) and aqueous ($\alpha = 0$). The third term on the right hand side of Equation 1b is equal to zero when the flow is incompressible, i.e. Equation 1a is satisfied, and is added for numerical stability [31]. The body force term f_e represents the drag force imparted onto the fluid from the movement of charged particles and is defined as $f_e = \sum_{i=1}^{i=n} F c_i z_i \nabla \phi$. This body force is a simplification of the more general Lorenz force [32] by disregarding effects from magnetic fields, which is commonly done for ions in solution. To improve stability of the numerical solution and coupling between the membrane and water phase, the simulation domain is monothetic with ion selectivity modeled through single ion partition coefficients and the mass transfer model from Haroun et al. represented by Θ in Equation 1e [33]. Originally formulated to enforce non equal partitioning of gases (Henry's law), Haroun's mass transfer model ensures mass conservation at phase boundaries and enforces the jump condition that occurs with non-equal partitioning of ions, i.e., the ratio of ions present in the water (c_{aq}) and membrane phases (c_{mem}) are non unity $\frac{c_{aq}}{c_{mem}} = k \neq 1$ [33]. The additional flux (Θ), referred to as the "solubility flux", acts to counteract the nonphysical diffusive flux that would arise from a concentration jump at interfaces, where $\nabla \alpha \neq 0$. At thermodynamic equilibrium, when $c_{aq} = k c_{mem}$, the solubility flux (Θ) is equal in magnitude to the diffusive flux at the interface when central discretization schemes are used regardless of the mesh size near the interface [33]. This interface model is similar to the traditionally used Chang-Jaffe boundary conditions assuming diffusion limited surface reactions, but with the added benefit of a singular domain to describe the NPP equations. To our knowledge, this approach, which has been successfully employed in gas partitioning into liquids [34, 35], has not employed in conjunction with the NS-NPP equations previously, and has not been employed in examining ion selectivity across phase boundaries. We also note that here binary values of α are employed, but more general α can be treated as a phase fraction and the

Table 1 Mathematical description of the boundary conditions as labeled in 1a with n representing the face normal direction and I the identity matrix. The subscripts f and p signify the value at the boundary face and neighboring cell, respectively.

Boundary	Ions (c_i)	Potential (ϕ)	Velocity ($\vec{U}$)	Pressure (P)
1	$\frac{\partial c_i}{\partial n}_f = 0$	$\frac{\partial \phi}{\partial n}_f = 0$	$\vec{U}_f = (1,0,0)$	$\frac{\partial P}{\partial n}_f = 0$
2	$\frac{\partial c_i}{\partial n}_f = 0$	$\frac{\partial \phi}{\partial n}_f = 0$	$\frac{\partial \vec{U}}{\partial n}_f = 0$	$\frac{\partial P}{\partial n}_f = 0$
3	$\frac{\partial c_i}{\partial n}_f = 0$	$\frac{\partial \phi}{\partial n}_f = 0$	$\frac{\partial \vec{U}}{\partial n}_f = 0$	$P_f = 0$
4	$\frac{\partial c_i}{\partial n}_f = 0$	$\frac{\partial \phi}{\partial n}_f = 0$	$\vec{U}_f = \frac{1}{2}(\vec{U}_p + (I - 2nn^T)\vec{U}_p)$ *	$\frac{\partial P}{\partial n}_f = 0$
5	$\frac{\partial c_i}{\partial n}_f = 0$	$\frac{\partial \phi}{\partial n}_f = 0$	$\vec{U}_f = (0,0,0)$	$\frac{\partial P}{\partial n}_f = 0$
6	$\frac{\partial c_i}{\partial n}_f = 0$	$\frac{\partial \phi}{\partial n}_f = 0$	–	–
Membrane-Water Interface	–	–	$\vec{U}_f = (0,0,0)$	$\frac{\partial P}{\partial n}_f = 0$

approach applied here can be extended to mixtures unlike the Chang-Jaffe boundary condition.

B. Domain and Boundary Conditions

In lieu of modeling a complete ISE sensor geometry, we base our model off of classical boundary layers with a leading edge, as the fluid flow and shear stress in the absence of ion migration and electrostatic body forces are well known in this scenario. The specific computational domain employed is a 2D representation of flow over a flat membrane and is shown in Figure 1. Here the numerical solution of the NS equations (U and P) is restricted to only the white region labeled "Water" in 1a. The electric potential (ϕ), a continuous variable, is solved for in both the aqueous phase and the membrane phase (shaded gray in 1b) without distinction between phases, as we modeled both phases with the same electrical permittivity. The species concentration (c_i) is also solved for in both the aqueous phase and membrane phase, but accounting for partitioning at the water-membrane interface via Haroun's solubility flux approach [33]. The same computational mesh was used for both the global domain, comprising of the aqueous and membrane phase, as well as the aqueous phase. Therefore, the fluid properties solved within the separate water subdomain are easily mapped to the global domain for solution of Equation 1d. In Figure 1a, each boundary is labeled and the corresponding boundary conditions may be found in Table 1. The domain was made sufficiently large such that the effect of boundary conditions, namely the zero gradient condition on the potential, would not affect the results near the ISE membrane and aqueous sample interface. The computational mesh was designed using hanging nodes and successive refinement to ensure high spatial resolution near the membrane and fluid interface without compromising the overall simulation cost, particularly as the unsteady nature of this simulation and highly coupled equations make computational cost high. The mesh selected had $4.3 \cdot 10^5$ hexahedral cells and is shown in Figure 1b.

*The boundary condition at Boundary 4 is commonly referred to as the symmetry condition. The implementation of this boundary condition for multi-dimensional variables such as U is the mean of the adjacent cell and the mirror image produced by the Householder transformation. [36]

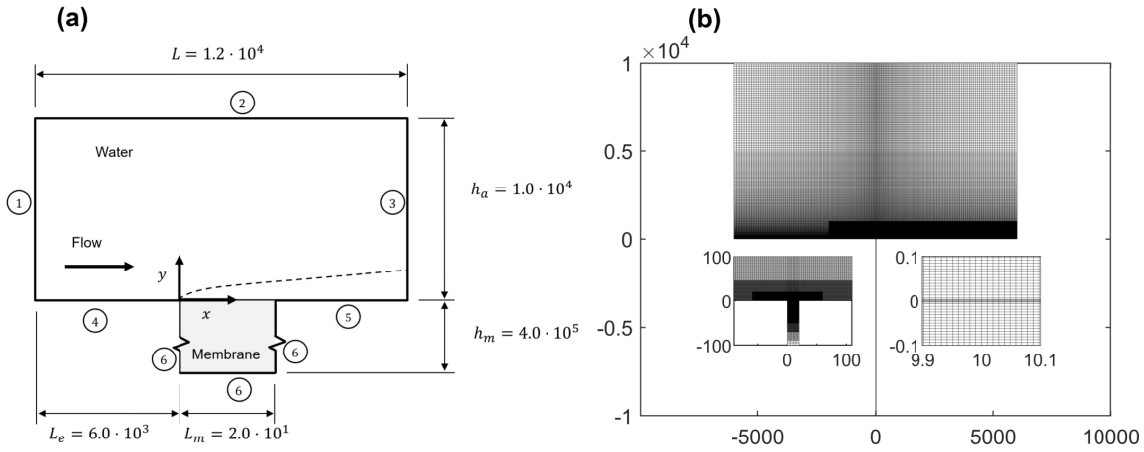

Fig. 1 Schematic of the computational domain of a liquid flow over an immiscible membrane phase. (a) Dimensions and labeled boundaries, with more details provided in Table 1. (b) Computational mesh used in this study, with insets providing higher magnification of the ISE membrane and aqueous sample interface. All units presented in this figure are dimensionless, with the dimensionless length scale defined as $x^* = \frac{xU_0}{\nu}$. More information about the non-dimensionalization procedure can be found in the Theory and Solution Scheme section.

C. Numerical Solution Scheme

A custom C++ program was developed to solve Equations 1a-e using the finite volume method and open source library OpenFOAM. This library abstracts many of the aspects of finite volume discretization and subsequent matrix construction and numerical solution. This allows developers to focus on higher level solution algorithms and add additional transport equations such as those present in the NS-NPP equations. To solve the coupled system of Equations 1a-e for the dependant variables $U, P, \phi, c_0, c_1, ...$ and c_i, a modification to the PISO algorithm [28] to include the NPP equations along with an embedded singly-diagonal implicit Runge-Kutta(SDIRK) [37] time discretization is used. Time steps are varied using a PPID time step controller[38] with a desired normalized numerical solution error of $1 \cdot 10^{-6}$. More information on the specific implementation of time step control is included in the supporting information. Within the PISO algorithm, a sub loop for the Nernst-Planck equation coupling with the Poisson equation is solved using the semi-implicit algorithm from Hagelaar et al. [29]. The modified PISO algorithm implemented along with the implementation of Hagelaar's method is shown in Algorithm 1.

To explain the modifications to the PISO algorithm, the notation used is consistent to what is largely used by the OpenFOAM community and can be found in detail within Jasak's PhD thesis [39]. For brief explanation of the notation, the H operator includes all off diagonal components of the discretized momentum equation (Equation 1b) along with any explicit source terms arising from boundary conditions and time discretization methods. The a coefficient represents the diagonal components of the discretized momentum equation. All iterative values, n, i, j, k in Algorithm 1 use superscripts with parenthesis () to indicate iteration steps, and brackets [] to indicate the SDIRK stage. The

algorithm begins by calculating the fluid variables (U and p) with the standard PISO algorithm implementation as is done within OpenFOAM's solver pisoFOAM with the addition of the electrostatic body force, which is calculated explicitly by values from previous iterations. Following the computation of U and p, the electrostatic potential and species concentrations are solved using Hagelaar's algorithm without update to fluid variables U and p. The Algorithm ends with another iteration of the PISO algorithm, but this time with updated values for ϕ and c. The Algorithm was structured such that the variables with the strongest coupling, such as the pairs U and p and ϕ and c, have adequate convergence before incorporating the weaker, but still prevalent, body force term that couples the fluid variables to the species transport. The "stop" condition for each loop is based on convergence of the resulting linear systems for Equations 1a-e. The convergence is determined based on the L_1 norm of the matrix residuals and is defined as $r = \frac{1}{\sum(|Ax - A\bar{x}| + |b - A\bar{x})} \sum |b - Ax|$ where A and b are the coefficient matrix and source term produced from the finite volume and time discretization of the variable x with $\bar{x}$ representing the average value of x. Convergence was determined when the L_1 norm was at or bellow $1 \cdot 10^{-6}$ before exiting the iteration loops presented in Algorithm 1.

For the spatial discretization, built-in functionality of OpenFOAM's matrix constructors were employed. For all transport equations, divergence operators were discretized using 1st order upwind methods, while gradient operators used Gaussian integration with 2nd order linear interpolation without non-orthogonal or skewness corrections. This solver uses a custom time discretization following the work of Dalessandro et al.[40] for incorporating SDIRK methods into OpenFOAM. The specific method used was a 3rd order 3 stage embeded SDIRK method with a 2nd order error estimator from Alexander[37]. For the special case of solving the Poisson equation with only Neumann boundary conditions (electric field equal to zero on all boundaries), the fixed point method [41] is applied. Here the compatibility condition and fixed point value are enforced by modifying the resulting matrix equation from the discretization of Equation 1c by solving the modified linear system $A^{'}x = b^{'} - \bar{b^{'}}$ where $A' = A + A(i,i)$ and $b^{'} = b + A(i,i)\phi_{ref}$. Here i represents the cell location of the fixed value (ϕ_{ref}) and $\bar{b^{'}}$ is the average of the matrix source term $b^{'}$. For further details of implementation, the complete code is linked in the supporting information.

The order of the numerical solution was inspired by Oliveira's PISO extension for buoyancy driven flows [42] where similarly the NS equations are modified to include a body force derived from a scalar transport equation, in Oliveira's case the heat equation and here the Poisson equation, which in turn is influenced by the ion transport equation. While the exact solution order may affect stability and convergence rates, the proposed algorithm was deemed suitable for the present study and has been validated with a series of analytical, experimental and prior numerical studies. The first comparison is to experimental measurements of the velocity profile in an electrostatic precipitator, where the velocity is influenced by the electrostatic body force [43] and hence its determination requires solution to the NS-NPP set of equations. The second is a comparison to Schönke's [44] analytical solution for the NPP set of equations, testing our ability to recover solutions with coupled mass transfer and electrostatics. The third is recovery of the classical Blasius solution for boundary layers of a flat plate. In the absence of electrostatic effects, for the geometry tested here (Figure

Algorithm 1 Segregated solver for the numerical solution to the coupled NS-NPP equations.

$n \leftarrow 1$
while RK loop **do**
  $i \leftarrow 1$
  while U,P,ϕ,c_0,c_1,...c_i are not converged **do**
    $j \leftarrow 1$
    while U,P are not converged **do**
      $U^{(j+1)} \leftarrow \frac{\partial U}{\partial t}^{[n]} + U^{(j)}\nabla \cdot U^{(j+1)} = -\nabla P^{(j)} + \nu\nabla^2 U^{(j+1)} + \nabla\frac{\phi^{(i)}}{\rho}\sum_{s=1}^{S} e z_s c_s^{(i)}$ ▷ Solve Predictor step
      $P^{(j+1)} \leftarrow \nabla \cdot \frac{1}{a}\nabla P^{(j+1)} = \nabla \cdot \frac{H(U^{(j+1)},\phi^{(i)},c_i^{(i)})}{a}$ ▷ Solve Pressure Equation
      $U^{(j+2)} \leftarrow \frac{H(U^{(j+1)},\phi^{(i)},c_i^{(i)})}{a} - \frac{1}{a}\nabla P^{(j+1)}$ ▷ Corrector Step
      $j \leftarrow j + 1$
    end while
    $k \leftarrow 1$
    while ϕ,c_0,c_1,...c_i are not converged **do**
      if j == 1 **then**
        $\beta \leftarrow \epsilon + \sum_{s=1}^{S} z_s^2 \delta t c_s^{[n]}$
        $\phi^{(k+1)} \leftarrow \nabla \cdot \beta\nabla\phi^{(k+1)} = \sum_{s=1}^{S} z_s c_s^{[n]} F + \sum_{s=1}^{S} F z_s \delta t(\frac{\partial c_s}{\partial t}^{[n]} - z_s c_s^{[n]} \frac{FD_s}{RT}\nabla\phi^{[n]})$ ▷ Voltage Predictor
      else
        $\phi^{(k+1)} \leftarrow \nabla \cdot \epsilon\nabla\phi^{(k+1)} = \sum_{s=1}^{S} z_s c_s^{[n]} F$
      end if
      $c^{(k+1)} \leftarrow \frac{\partial c}{\partial t}^{[n]} + \nabla \cdot (c_i^{(k+1)}[z_i \frac{FD}{RT}\nabla\phi^{(k+1)} + U^{[n]} + \frac{D_i(1-k_i)}{\alpha+k_i(1-\alpha)}\nabla\alpha]]) = \nabla \cdot D\nabla c_i^{(k+1)}$
      $k \leftarrow k + 1$
    end while
    $j \leftarrow 1$
    while U,P are not converged **do**
      $U^{(j+1)} \leftarrow \frac{\partial U}{\partial t}^{[n]} + U^{(j)}\nabla \cdot U^{(j+1)} = -\nabla P^{(j)} + \nu\nabla^2 U^{(j+1)} + \nabla\frac{\phi^{(i+1)}}{\rho}\sum_{s=1}^{S} e z_s c_s^{(i+1)}$ ▷ Solve Predictor step
      $P^{(j+1)} \leftarrow \nabla \cdot \frac{1}{a}\nabla P^{(j+1)} = \nabla \cdot \frac{H(U^{(j+1)},\phi^{(i+1)},c_i^{(i+1)})}{a}$ ▷ Solve Pressure Equation
      $U^{(j+2)} \leftarrow \frac{H(U^{(j+1)},\phi^{(i+1)},c_i^{(i+1)})}{a} - \frac{1}{a}\nabla P^{(j+1)}$ ▷ Corrector Step
      $j \leftarrow j + 1$
    end while
    $i \leftarrow i + 1$
  end while
  $n \leftarrow n + 1$
end while

1), simulations recover the Blasius solution, showing that the flow modeled is a viscous boundary layer flow in the developing region. Validation results can be found in the supplemental material. Further validations more specific to ISEs are discussed in the Results and Discussion section [11]. Simulations were run on a Minnesota Supercomputing Institute (MSI) cluster utilizing 8 cores for each simulation and requiring roughly 120 hours of run time for each case noted in the subsequent section.

D. Non-Dimensionalization and Test Cases

To reduce the number of independent parameters affecting fluid flow and transport of charged ions in solution, we adopt a non-dimensionalization conventionally utilized in studying boundary layer formation from external flow of a viscous fluid over a surface [45]. We define the non-dimensional length scale as $x^* = \frac{xU_0}{\nu}$ where U_0 is the bulk fluid velocity and x the spatial dimension, the non-dimensional time scale as $\tau = \frac{t\nu}{U_0^2}$ and the non-dimensional velocity as $U^* = \frac{U}{U_0}$. This variable transformation fixes fluid behavior to problem geometry (x^*) and time scale (τ), allowing for examination of other transport phenomena, such as ion motion within the formed fluid boundary layer, with fixed fluid characteristics. We correspondingly define the non-dimensional potential as $\phi^* = \phi\frac{Fc_0}{\rho_f U_0^2}$ where c_0 is the reference ion concentration and the non-dimensional concentration as $c^* = \frac{c}{c_0}$. This combination of fluid and electrochemical variable transformations leads to the non-dimensionalization of Equations 1a-e as:

$$\nabla \cdot \vec{U}^* = 0 \tag{2a}$$

$$\frac{\partial \vec{U}^*}{\partial \tau} + \vec{U}^*\nabla \cdot \vec{U}^* = -\nabla P^* + \nabla^2\vec{U}^* + \nabla \cdot [(\nabla\vec{U}^*)^T - \frac{2}{3}(\nabla\vec{U}^*)] + \sum_{i=1}^{i=n} c_i^* z_i \nabla\phi^* \tag{2b}$$

$$\nabla^2\phi^* = \frac{1}{Re_{db}^2\psi_f}\sum_{i=1}^{i=n} c_i^* z_i \tag{2c}$$

$$\frac{\partial c_i^*}{\partial \tau} + \nabla \cdot (c_i^*[\vec{U}^* + z_i\frac{\psi_f}{Sc_i}\nabla\phi^* + \Theta^*]) = \frac{1}{Sc_i}\nabla^2 c_i^* \tag{2d}$$

$$\Theta^* = \frac{1}{Sc_i}\frac{(1-k_i)}{\alpha + k_i(1-\alpha)}\nabla\alpha \tag{2e}$$

$$\tag{2f}$$

where the resulting dimensionless parameters are the fluid kinetic to chemical potential energy ratio $\psi_f = \frac{\rho_f U_0^2}{c_0 RT}$, the ion Schmidt number $Sc = \frac{\nu}{D}$ and the Debye-length Reynolds number $Re_{db} = \frac{U_0\lambda_{db}}{\nu}$ with the Debye length $\lambda_{db} = \sqrt{\frac{\epsilon RT}{F^2 c_o}}$. The Debye-length Reynolds number determines the relative strength of the fluid flow inertia within one Debye length of the fluid-membrane interface. When Re_{db} is large ($Re_{db} >> 1$), significant changes to ion transport rates, driven by fluid flow, occur in the region most sensitive to changes in electrostatic potential. Conversely, when Re_{db} is small ($Re_{db} << 1$), electrostatic forces dominate ion transport, i.e., convection has little influence on transport at the membrane interface. As will be seen in later sections, this parameter will be paramount to exploring the effects

of fluid flow on partitioning of ions across the membrane-water interface. Dimensionless numbers associated with membrane and ion transport found in prior work [11] (i.e., when solving the NPP equations) can be defined from this set of non-dimensional parameters, including the dimensionless potential $\psi_f \phi^* = \phi \frac{F}{RT}$, dimensionless length scale $\frac{x^*}{Re_{db}} = \frac{x}{\lambda_{db}}$ and dimensionless time scale $\frac{\tau}{ScRe_{db}^2} = \frac{tD}{\lambda_{db}^2}$. These dimensionless ratios will be used in the subsequent sections for analyzing the mass transfer of ions and associated changes in the potential across the membrane-water phase boundary.

A series of simulations where preformed varying Sc, Re_{db} and ψ_f for a binary salt solution. To accomplish this using the code developed for Equations 1a-e, variables ν, c_0, U and ρ_f were set to 1 m^2s^{-1}, 1 mol m^{-3}, 1 m s^{-1} and 96485 kg m^{-3} (having the same magnitude as Faraday's constant) respectively. The remaining three variables, i.e., D_i, ϵ and T, were modulated to represent Sc, Re_{db} and ψ_f. For each case the non-dimensional ion concentration (c^*) was initialized as a constant value of 1.0 in both the membrane and water phases for the cation (+1 charge) and anion (-1 charge). Similarly, the non-dimensional velocity (U^*) was set to a magnitude of 1 with a direction parallel to the plate. For a test of this model, it was assumed here that the ion diffusion coefficient varied neither in space or phase and that it was the same between the anion and cation. Permittivity (ϵ) was also held constant throughout the domain irrespective of phase. For all cases the single ion partition coefficients (k_i) were held constant with a value of 2 (hydrophilic) for the cation and 0.5 (hydrophobic) for the anion, similar to parameters used by [11] in examining transport across an interface. To ensure accurate capture of the thin double layer, the mesh was designed to have a cell thickness at the phase boundary of no more than $0.02\lambda_{db}$ when $Re_{db} = 0.1$, noting that the mesh and dimensions of the membrane are scaled based on fluid properties and not the Debye length. To test mesh quality, a secondary mesh with resolution of $1.5 \cdot 10^6$ hexahedral cells and fa phase boundary cell thickness of no more than $0.01\lambda_{db}$ was run for two selected cases ($Re_{db} = 1$, $\psi_f = 1$, $Sc = 1000$ and $Re_{db} = 0.1$, $\psi_f = 1$, $Sc = 1000$). The potential between these two mesh resolutions varied no more than 1% when $\frac{\tau}{ScRe_{db}^2} > 1$. Therefore, the first mesh with $4.3 \cdot 10^5$ cells depicted in Figure 1b was used for the remainder of the study.

III. Results and discussion

In the absence of external flow (i.e, when $Re_{db} = 0$) or when flow is negligible, a double layer is formed and the resulting potential arises from the non-equal partitioning of ions. This potential can be predicted at the $t \rightarrow \infty$ limit by recognizing that, at equilibrium, the electrochemical potential of each ion is the same in both phases. For a binary electrolyte consisting of monovalent ions, this can be formulated to be a function of the single ion partition coefficients, and is defined as [11, 46]

$$\Delta(\psi_f \phi^*) = \frac{1}{2} ln \left(\frac{k_+}{k_-} \right) \tag{3}$$

where k_+ and k_- are the single ion partition coefficients of the cation and anion, respectively. Prior research has shown that Equation 3 accurately describes the phase boundary potential at the $t \rightarrow \infty$ limit when the diffusion potential, often referred to as the Henderson potential, is negligible, i.e., when the partitioning ions have the same diffusion coefficient [11, 47]. To demonstrate this and to provide code validation, we compare the temporal evolution of the phase boundary potential with the expected value obtained from Equation 3 for the case of no-flow. Figure 2a shows that when $tD/\lambda_{db}^2 > 1$ the potential converges to the predicted value from Equation 3. We observe that the evolution of the phase boundary potential is clearly divided into a a dynamic phase for $tD/\lambda_{db}^2 < 1$ and an effectively static phase at $tD/\lambda_{db}^2 > 1$, suggesting that the use of tD/λ_{db}^2, which is equivalent to $\frac{\tau}{ScRe_{db}^2}$, is a well-scaled dimensionless time for these systems and is henceforth used to present temporally-varying results. For additional validation, the ion concentration profiles near the ISE membrane and aqueous sample interface at $tD/\lambda_{db}^2 = 10$ are compared with the results obtained from Zhurov et al. [11] in Figure 2b for the case where $k_+ = 2$ and $k_- = 0.5$. We apply these same partition coefficients here and throughout this study. However, specific to this validation, we employ $Sc = 3.98$ for the cation and $Sc = 1$ for the anion in order to match the conditions from Zhurov et al. The concentration profiles for both the cation and anion in Figure 2b show a high degree of symmetry as in the absence of flow, ion motion is dominated by near interface electric fields and concentration gradients, which are independent between phases for this problem set up. The strong agreement here, demonstrates simulations correctly capture ion diffusive and electrophoretic motion as well as the development of a space-charge induced electrostatic potential field. Additional validations are provided in the supporting information, including comparison to classical boundary layer results, comparison to analytical NPP equation solutions and comparison with experimental electrohydrodynamic flow velocity measurements.

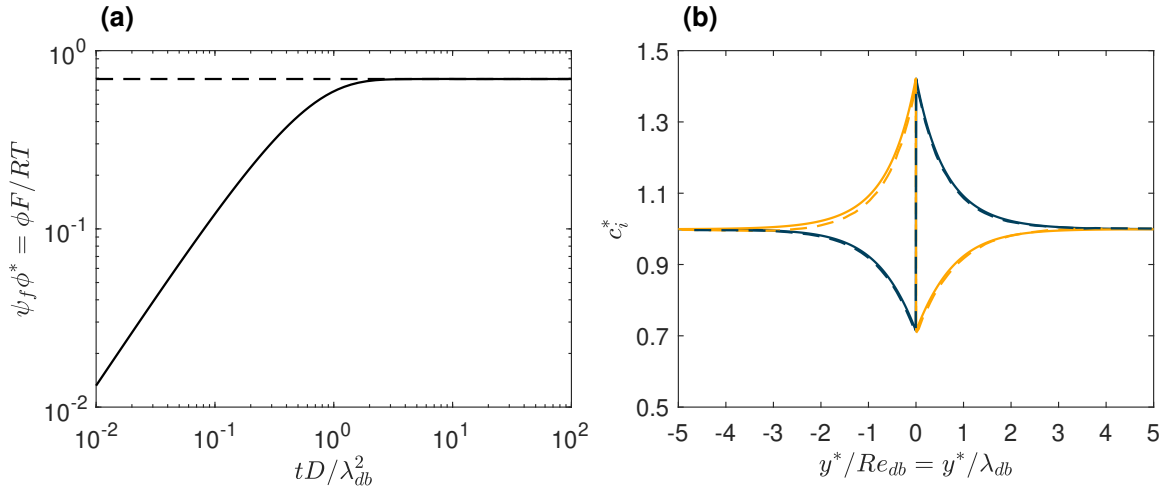

Fig. 2 Results for the no-flow case ($\psi_f = 1$, $Sc = 1000$, $Re_{db} = 0$). (a) Temporal evolution of the phase boundary potential (solid black line) compared to expected potential from Equation 3 (dashed black line). (b) Concentration profiles of Cation (blue) and Anion (yellow) with comparison between the current study (solid) and results from Zhurov et al. [11] (dashed). Quantities where taken from the midpoint location of membrane, $x^* = 5$, with the ISE membrane and aqueous sample interface at $y^* = 0$ and at a time of $tD/\lambda_{db}^2 = 10$. Information on the Domain used refer to Figure 1.

Adding external flow to this system, Figure (3) displays a series of cation and anion concentration maps for variable Debye Length Reynolds numbers, with fixed ψ_f, which is the dimensionless parameterization of ion mobility, and fixed Sc, the dimensionless parameterization of ion diffusivity. The case shown in Figures (3a) (cation) and (3e) (anion), with a $Re_{db} = 0.1$, shows concentration profiles mostly unaffected by external flow; this case is similar to the validation case presentation in Figure 2b. The concentration boundary is confined to the narrow region close to the membrane with near-lateral symmetry. However, with increasing Re_{db}, analogous to the boundary layer formed for similar problems of forced convection on surfaces, fluid flow increases ion concentration gradients near the fluid-membrane interface, particularly at the leading edge, as is evident in Figures (3b-d) and (3f-h), and leads to formation of a growing boundary layer. As Re_{db} tends to unity, fluid flow effects on the boundary are pronounced, with noticeable ion concentration variation at y^*-locations near 1.0, in comparison to the boundary layer in the absence of fluid flow of order 0.01 in thickness.

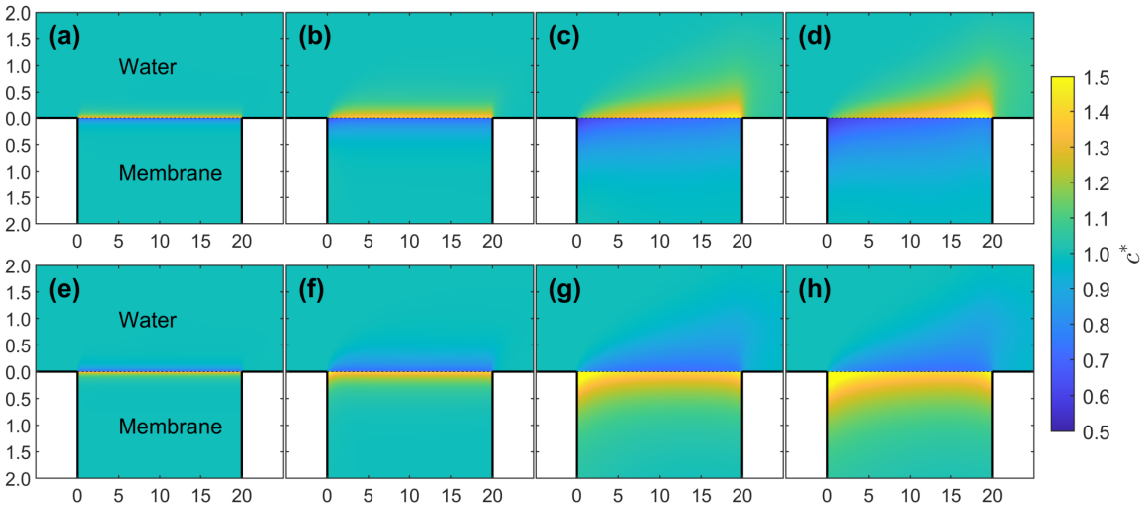

Fig. 3 Spatial distribution of dimensionless ion concentration c_i^* near the ISE membrane and aqueous sample interface at a time of $\frac{\tau}{ScRe_{db}^2} = 10$ for the cations (a-d) and anions (e-h) with single ion partition coefficients of 2.0 (cation) and 0.5 (anion) as well as $\psi_f = 1$ and $Sc = 1000$. From Left to right, varying Re_{db} with $Re_{db} = 0.1$ (a and e),$Re_{db} = 0.3$ (b and f),$Re_{db} = 0.8$ (c and g) and $Re_{db} = 1.0$ (d and h). All spatial dimensions are non-dimensional defined by Equation 2. The black dashed line represents the phase boundary.

The differences between the low flow velocity ($Re_{db} = 0.1$) and high flow velocity cases ($Re_{db} = 1$) are also demonstrated by profile data at $x^* = 5$ as shown in Figure 4a. This x^* location is selected intentionally to be close to the leading edge of the membrane, but sufficiently distal to avoid the influence of edge effects. We specifically plot ion concentration as a function of y-location normalized by the Debye length, which is the product of y^* and Re_{db} in the employed dimensionless framework. The low Re_{db} (dashed lines in Figure 4a) hence leads to concentration boundary layers of length near unity, i.e., similar in thickness to the Debye length. As Re_{db} increases to 1.0 (solid lines in Figure 4a) the encroachment of the fluid boundary layer within 1 Debye length of the interface leads to a small, but

noticeable decrease in the thickness of the charge separation layer in the fluid phase (when normalized by the Debye length). In in Figure 4b we plot the total charge density (dimensionless) as a function of $y^* Re_{db}^{-1}$ across the membrane and aqueous phase, as well as the dimensionless potential ($\psi_f \phi^*$) across the interface. This subtle asymmetry brought about by flow leads a pronounced increase in the potential at distance larger than the Debye length. Insets in Figure 4b nonetheless show that the potential reach a near constant value close the membrane interface (i.e. after several Debye lengths), hence the main effect is to increase the phase boundary potential.

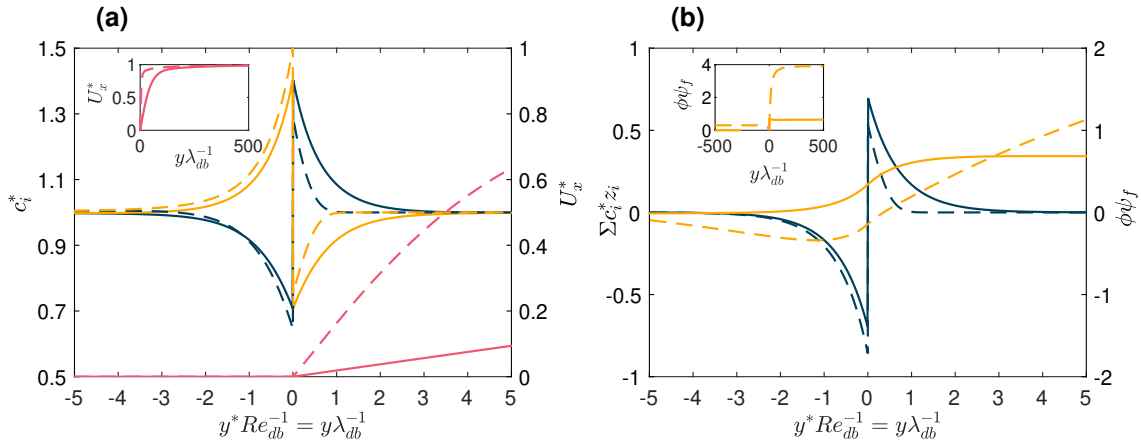

Fig. 4 Quantities of interest at varying $y*$, with the ISE membrane and aqueous sample interface occurring at $y^* = 0$, taken from a location within the membrane, $x^* = 5$, for $\psi_f = 1$, $Sc = 1000$, $Re_{db} = 0.1$ (dashed lines) and $Re_{db} = 1.0$ (solid lines). (a) Dimensionless charge concentration (blue) and dimensionless electric potential $\phi\psi_f$ (yellow) varying over dimensionless length (scaled by Debye length). (b) Dimensionless concentration for cation (blue) anion(yellow) and dimensionless velocity ($U^* = U/U_0$) varying over dimensionless length (scaled by Debye length).

In Figure 5 we plot the temporal evolution (with tD/λ_{db}^2 again as the dimensionless time) of the phase boundary potential for variable combinations of ψ_f and Sc and Re_{db} varying from 0.1-1.0. In all cases, similar to zero flow condition, we observe dynamic and static regions, separated by tD/λ_{db}^2 near unit value. Interestingly at small times, independent of Re_{db}, ψ_f, and Sc. the phase boundary potential increases with tD/λ_{db}^2 scaled to the power of 1, suggesting early time behavior is completely diffusion limited. With increasing Re_{db} in all cases we observe changes in both the dynamic regime and the static regime. In the dynamic regime, the phase boundary potential begins to increase more rapidly at higher Re_{db} for tD/λ_{db}^2 beyond 10^{-1}, with a scaling exponent approaching 1.6 for $Re_{db} = 1.0$, $\psi_f = 1.0$ and $Sc = 1000$, suggesting that fluid flow influences become significant as the system approaches the static regime. In the static regime, small values of Re_{db} have minimal effect on the phase boundary potential, but for the highest Re_{db} values examined we observe instances where the potential is than three times its expected value in the absence of flow (denoted via horizontal lines in Figure 5).

The change in the phase boundary potential with Re_{db} is highly dependent upon the values of ψ_f and Sc as is evident in Figure 6, where we plot the potential in the static limit. Specifically, results apply when $tD/\lambda_{db}^2 = 10$. For

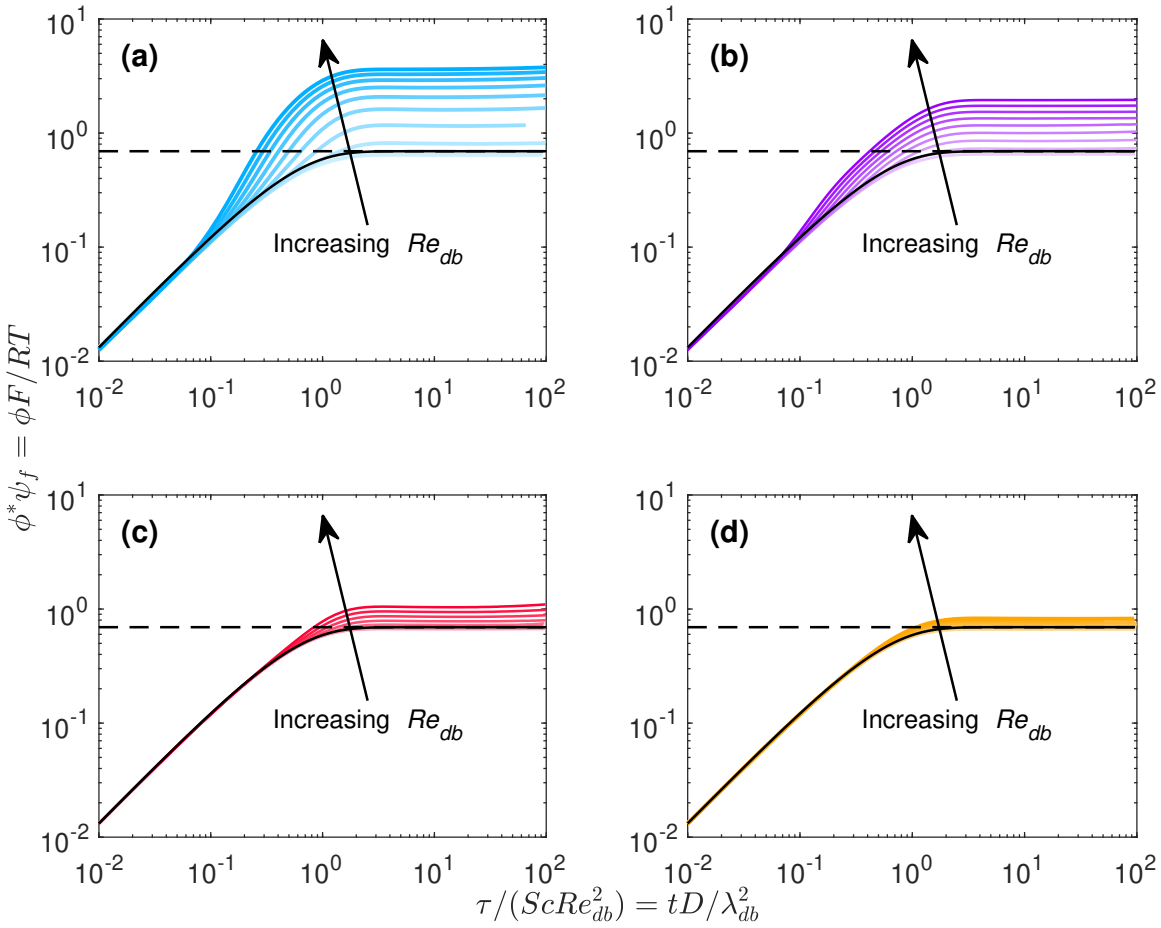

Fig. 5 Dimensionless potential temporal evolution with varying Re_{db} (Range of 0.1 to 1 in increments of 0.1 indicated by varying color saturation) with (a) $\psi_f = 1$ and $Sc = 1000$ (b) $\psi_f = 1$ and $Sc = 100$ (c) $\psi_f = 0.1$ and $Sc = 1000$ (d) $\psi_f = 0.1$ and $Sc = 100$. Results are plotted along side the potential predicted by Equation 3 (dashed black line) and the no-flow case, $Re_{db} = 0$, from Figure 2 (solid black line).

the case of $\psi_f = 0.1$ and $Sc = 100$, the effect of Re_{db} on the static potential is minimal, with the potential increasing from a value of 0.69 at $Re_{db} = 0.1$ to a value of 0.83 at $Re_{db} = 1$. For the case of $\psi_f = 1$ and $Sc = 1000$, the effect of Re_{db} on the static potential is more substantial, with the potential increasing to a value of 3.6 at $Re_{db} = 1$. Both Sc and Re_{db} parameterize the extent with which external flow affects the diffuse ionic double layers near the membrane-water interface; higher Sc diminishes ion diffusion in comparison to flow, while higher Re_{db} diminishes space charge induced potential effects. ψ_f, the ratio of the fluid kinetic energy to system characteristic electrostatic energy, serves as an amplification factor, increasing the extent that flow-ion interaction has on the phase boundary potential. To more clearly discern fluid flow effects and better define the influence of each dimensionless ratio, we introduce the enhancement coefficient η, which compares the static portion of the potential ($\frac{\tau}{ScRe_{db}^2} >> 1$) to the expected potential in the case of no-flow from Equation 3:

$$\eta = \frac{2\phi^*\psi_f}{ln\frac{K_+}{K_i}} - 1; \tag{4}$$

An η of zero indicates no change in phase boundary potential from its zero-flow limit. The enhancement coefficient may be modeled as a function of the previously defined system parameters, namely Re_{db}, ψ_f and Sc, alongside dimensionless numbers parameterizing system length ratios and the properties of the fluid, membrane, and ions. We attempted to develop this function through two methods. First, following a trial-and-error route, we anticipate that the correlation for the enhancement coefficient will be functionally similar to heat and mass transfer coefficients, i.e., in the form of $\eta = \psi_f^{\alpha} f(Re_{db}^{\beta} Sc^{\gamma})$, where f is some function of $Re_{db}^{\beta} Sc^{\gamma}$ and α, β and γ are unknown fitting parameters. Fitting $\alpha = \frac{2}{5}$, $\beta = \frac{4}{5}$ and $\gamma = \frac{1}{3}$, we plot all results obtained in this study in Figure 7 with the ratio of η/ψ_f^{α} on the y-axis and $Re_{db}^{\beta} Sc^{\gamma}$ on x-axis. Plotted results are also provided in a table in the supporting information. To further determine the functional dependence of η on Re_{db} and Sc, we define the fluid scaling parameter $\omega_1 = Re_{db}^{\beta} Sc^{\gamma}$. When ω_1 is small, the transport of ions is dominated by diffusion having little influence from the fluid flow. Conversely, when ω_1 is large, ion transport is dominated by convective effects. Plotting $\eta\psi_f^{-\alpha}$ as a function of ω_1 in Figure 7, we find excellent collapse for all simulated conditions. We subsequently fit the collapsed result using the ratio of two power series in the form of $\eta\psi_f^{-2/5} = \frac{\sum_{i=0}^{N} a_i \omega_1^i}{\sum_{j=0}^{N-l} a_j \omega_1^j}$ where a_i are unknown coefficients and l determines the fitting behavior when $\omega \to \infty$; for example when $l = 1$, the fit equation reduces to a first order polynomial with a slope of $\frac{a^N}{a^{N-1}}$. We elect to use a value of $N = 4$ and $l = 1$ resulting in the following function

$$\eta = \psi_f^{2/5} \frac{a_1\omega_1^2 + a_2\omega_1^3 + a_3 a_4 \omega_1^4}{1 + a_5\omega_1 + a_6\omega_1^2 + a_4\omega_1^3} \tag{5}$$

where $a_1 = 1.92 \cdot 10^{-2}$, $a_2 = -1.47 \cdot 10^{-2}$, $a_3 = 0.68$, $a_4 = 4.3 \cdot 10^{-3}$, $a_5 = -0.212$ and $a_6 = 7.06 \cdot 10^{-3}$. Coefficients were obtained by the Curve Fitting Toolbox in MATLAB [48], and were selected because all values of $\omega_1 > 0$ produce a strictly positive enhancement $\eta > 0$, and they by definition lead to $\omega_1 \to 0$ as $\eta \to 0$ and also to $\eta \propto 0.68\omega_1\psi_f^{2/5}$ as $\omega_1 \to \infty$. Examining the data in Figure 7, we see a transition near $\omega_1 = 3$ where the effective enhancement ($\eta\psi^{-2/5}$) departs from a value near 0 to a near-linear scaling of 0.7 in the range of $5 < \omega_1 < 10$. Although some values of η are negative at small ω_1, we believe these to be caused by small numerical errors, and since their relative magnitude is close to 0, will treat such values as effectively zero. The existence of a transition between no enhancement ($\omega_1 < 3$) and linear scaling ($\omega_1 > 3$) suggests that there is a critical degree of ion advection, as characterized by ω_1, that must occur before the effect of external flow is to increase the phase boundary potential.

Membrane based ion-selective electrodes tend to have lower detection limits in the range of $1 \cdot 10^{-7}$ to $1 \cdot 10^{-6}$ M [49]. To put the above analysis of ω_1 into context we estimate that an external flow velocity of at least 16 cm s^{-1} is needed for $\omega_1 > 3$, assuming a $1 \cdot 10^{-7}$ M solution at room temperature (300K) and an ion diffusion coefficient of $1 \cdot 10^{-9}$ m^2 s^{-1}. This fluid velocity is well above the velocities encountered for such sensors in the majority of applications, which suggests that changes in phase boundary potential from external flow will only occur for very dilute systems and in the absence of a background electrolyte. The effects of varying single ion partition coefficients, variable

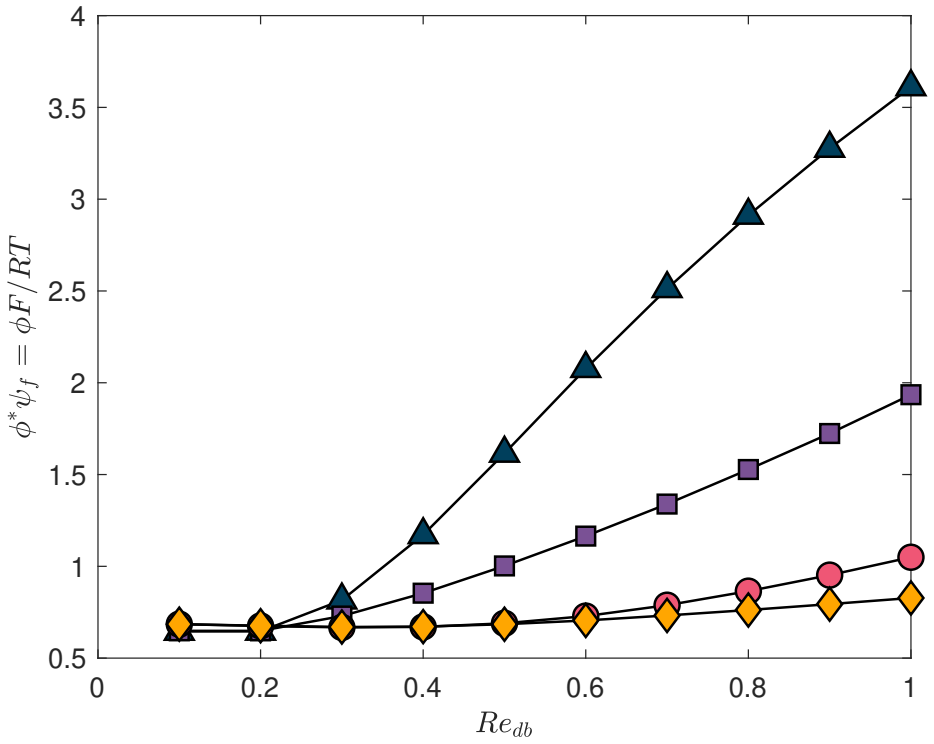

Fig. 6 Values at $\frac{\tau}{ScRe_{db}^2} = 10$ plotted for $\psi_f = 1$ and $Sc = 1000$ (blue triangle), $\psi_f = 1$ and $Sc = 100$ (purple square), $\psi_f = 0.1$ and $Sc = 1000$ (red circle) and $\psi_f = 0.1$ and $Sc = 100$ (orange diamond)

ion diffusion coefficients and variable ion concentrations in solution was not explored in this study, which may affect the exact limit at which external flow (ω_1) affects the phase boundary potential. Regardless, our results indicate that effects of external flow on membrane systems are more pronounced in the low concentration limit. This result is consistent with previous studies on reversed electrolysis cells were the greatest effect of flow on ion transport occurred for the smallest ion concentrations [9].

As a second approach to collapse results, we note that results do apply for the membrane which is of a specific length $L_m^* = 20.0$ (non-dimensionalized by $\frac{\nu}{U_0}$). To examine the interplay between different length scales affecting the problem, we define a dimensionless ratio $\omega_2 = \frac{\lambda_{db}}{\delta_m}$, where δ_m is a characteristic mass transfer layer thickness for the fluid after traveling a distance L_m (dimensional) along the membrane. δ_m can be defined as $\delta_m = \left(\frac{DL_m}{\lambda_{db}\gamma_s}\right)^{1/2}$, where γ_s is the characteristic shear rate. The shear rate, in turn, scales as $\gamma_s = \frac{U_0}{\delta_{mom}}$, with $\delta_{mom} = \left(\frac{L_m \nu}{U_0}\right)^{1/2}$. Combining these definitions yields:

$$\omega_2 = \frac{\lambda_{db}^{3/2} U_0^{3/4}}{D^{1/2} L_m^{3/4} \nu^{1/4}} \frac{\nu^{1/2}}{\nu^{1/2}} = Sc^{1/2} Re_{db}^{3/4} \left(\frac{\lambda_{db}}{L_m}\right)^{3/4} \tag{6}$$

Equation 6 leads to a similar functional form for ω_2 as empirically found for ω_1, but with an added term of $\frac{\lambda_{db}}{L_m}$ raised to the $3/4$ power. We plot $\eta\psi^{-2/5}$ versus ω_2 in Figure 8 for all test case performed here along side a line of best fit in the form of Equation 5. We retain the scaling of $\psi^{-2/5}$ as this find close to optimum in fitting. While the collapse of results

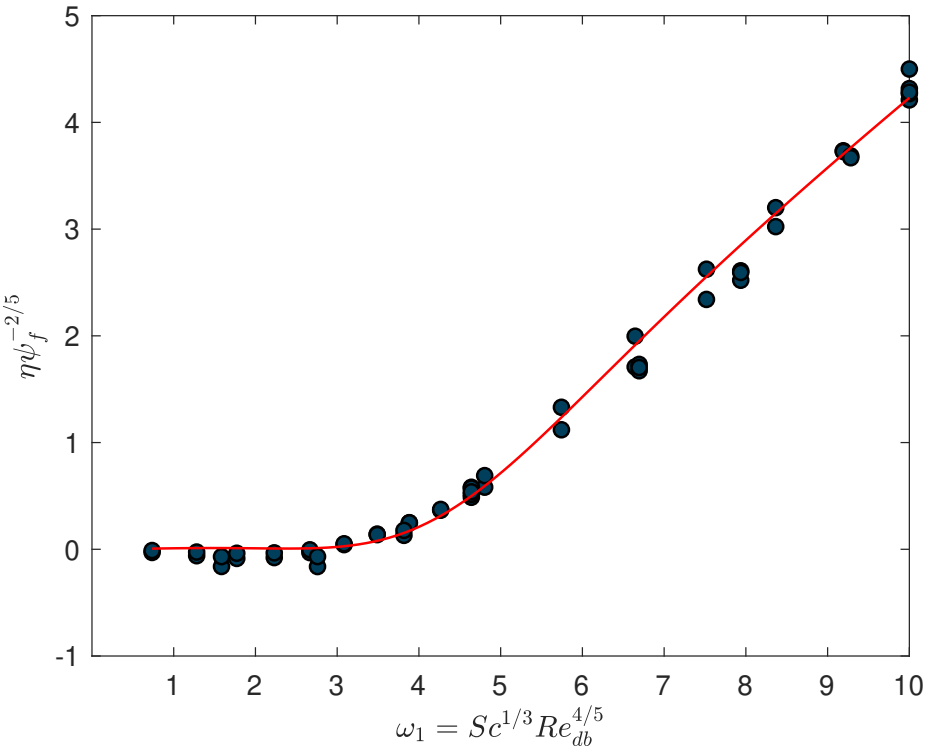

Fig. 7 Potential enhancement factor η scaled by $\psi_f^{-2/5}$ and plotted as a function of system Schmidt number (Sc) and Debye length Reynolds number (Re_{db}) for all data (blue circles). Data fitting is provided by Equation 5 and is shown as the red solid line.

is not as strong as the empirically-tuned result with ω_1, examination of ω_2 supports the scaling $\eta = \psi_f^{\alpha} f(Re_{db}^{\beta} Sc^{\gamma})$, and further suggests how results may be affected by adjusting the membrane length. Results would additionally be influenced by changes in ion partition coefficients for cationic and anionic species, as well as by utilizing unequal diffusion coefficients for species or unequal electrical permittivities for the fluid and membrane. For this reason, the solutions presented here cannot be considered universal, with additional simulations required to capture the influences of changing geometry,changing ion properties, and changing fluid and membrane electrical properties.

IV. Conclusion

We developed a code by modifying the open source library OpenFOAM to solve the Navier-Stokes-Nernst-Planck-Poisson set of equations to examine coupled mass transfer, fluid flow, and electrostatic potentials for non-equal partitioning ions at membrane-water interface. This code was used specifically to explore the effects of external viscous flow on the diffuse ionic double layers at the interface of an ISE membrane and aqueous sample and associated changes in phase boundary potential. Framing the problem in a manner similar to mass transfer in a developing boundary layer and utilizing an associated dimensionless framework revealed that the dimensionless numbers $\omega_1 = Re_{db}^{4/5} Sc^{1/3}$ or $\omega_2 = Re_{db}^{3/4} Sc^{1/2} \left(\frac{\lambda_{db}}{L_m}\right)^{3/4}$, which are functions of the Debye-length Reynolds Number and the Schmidt number, not

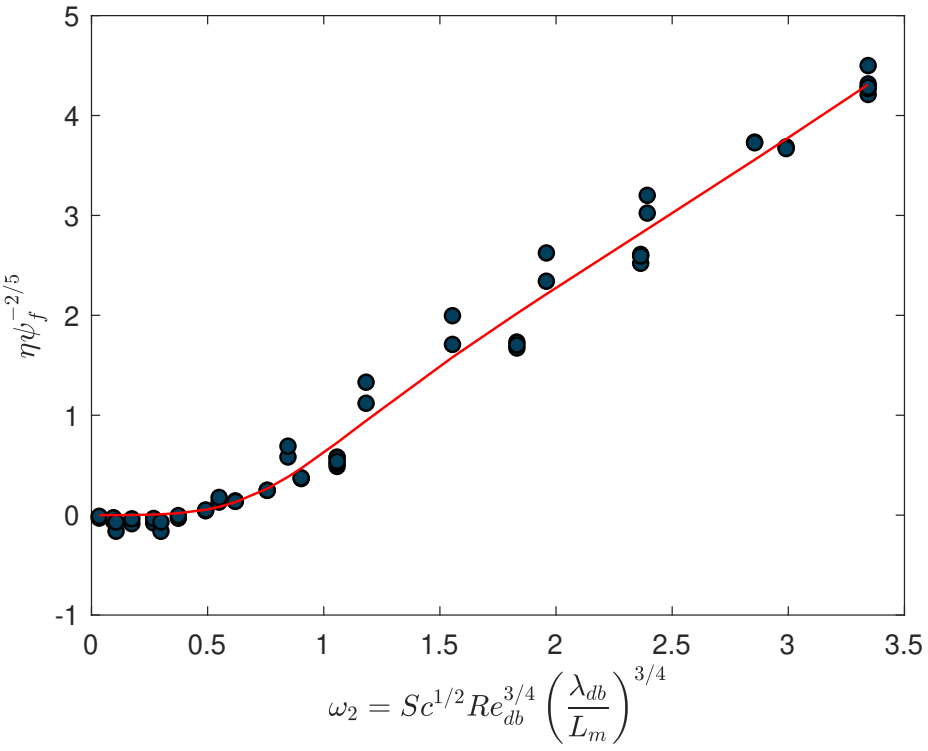

Fig. 8 Potential enhancement factor η scaled by $\psi_f^{-2/5}$ and plotted as a function of system Schmidt number (Sc) and Debye length Reynolds number (Re_{db}) for all data (blue circles) using the fluid scaling parameter ω_2 as defined in Equation 6. The red solid line represents data fitting by Equation 5 with coefficients $a_1 = 6.14 \cdot 10^{-3}$, $a_2 = 9.80 \cdot 10^{-2}$, $a_3 = 2.12$, $a_4 = 1.76 \cdot 10^{-1}$, $a_5 = -1.11$ and $a_6 = 6.98 \cdot 10^{-1}$.

only are appropriate metrics (switches) to determine if hydrodynamic forces affect the formation of the diffuse ionic double layers, but also can be used to quantitatively predict the extent to which fluid flow affects the phase boundary potential. Although this study focused on a sole geometry and set of partition concentrations, the results show the applicability of traditional heat and mass transfer analysis to describe ion transport at ISE membrane and aqueous sample interfaces in electrohydrodynamic flows, as it is relevant to ISEs and other system where phase boundary potential modeling is of interest.

V. Supplemental

A link to the Github repository for the code, implementation details for the time step controller, additional code validation cases, and tabulated data plotted in Figure 7 are available online.

VI. CRediT authorship contribution statement

A.J. Andrews: Conceptualization, Software, Formal analysis, Investigation, Methodology, Data curation, Writing - original draft, Writing - review & editing. P. Bühlmann: Conceptualization, Funding acquisition, Investigation, Writing - review & editing. C.J. Hogan: Conceptualization, Investigation, Methodology, Supervision, Writing - original draft,

Writing - review & editing.

VII. Acknowledgments

The authors acknowledge the Minnesota Supercomputing Institute (MSI) at the University of Minnesota for providing resources that contributed to the research results reported within this paper. P.B. acknowledges support by National Science Foundation Grant CHE-1748148 and CHE-2203752.

References

[1] Flagan, R. C., "History of Electrical Aerosol Measurements," *Aerosol Science and Technology*, Vol. 28, No. 4, 1998, pp. 301–380. https://doi.org/10.1080/02786829808965530.

[2] Mizuno, A., "Electrostatic precipitation," *IEEE Transactions on Dielectrics and Electrical Insulation*, Vol. 7, No. 5, 2000, pp. 615–624. https://doi.org/10.1109/94.879357.

[3] Wang, W., Luo, Q., Li, B., Wei, X., Li, L., and Yang, Z., "Recent Progress in Redox Flow Battery Research and Development," *Advanced Functional Materials*, Vol. 23, No. 8, 2013, pp. 970–986. https://doi.org/10.1002/adfm.201200694.

[4] Werber, J. R., Osuji, C. O., and Elimelech, M., "Materials for next-generation desalination and water purification membranes," *Nature Reviews Materials*, Vol. 1, 2016. https://doi.org/10.1038/natrevmats.2016.18.

[5] Bobacka, J., Ivaska, A., and Lewenstam, A., "Potentiometric Ion Sensors," *Chemical Reviews*, Vol. 108, No. 2, 2008, pp. 329–351. https://doi.org/10.1021/cr068100w.

[6] Bakker, E., Bühlmann, P., and Pretsch, E., "Polymer Membrane Ion-Selective Electrodes–What are the Limits?" *Electroanalysis*, Vol. 11, No. 13, 1999, pp. 915–933. https://doi.org/10.1002/(SICI)1521-4109(199909)11:13<915::AID-ELAN915>3.0.CO;2-J.

[7] Bakker, E., Bühlmann, P., and Pretsch, E., "The phase-boundary potential model," *Talanta*, Vol. 63, No. 1, 2004, pp. 3–20. https://doi.org/10.1016/j.talanta.2003.10.006.

[8] Sokalski, T., Ceresa, A., Zwickl, T., and Pretsch, E., "Large Improvement of the Lower Detection Limit of Ion-Selective Polymer Membrane Electrodes," *Journal of the American Chemical Society*, Vol. 119, No. 46, 1997, pp. 11347–11348. https://doi.org/10.1021/ja972932h.

[9] Długołęcki, P., Anet, B., Metz, S. J., Nijmeijer, K., and Wessling, M., "Transport limitations in ion exchange membranes at low salt concentrations," *Journal of Membrane Science*, Vol. 346, No. 1, 2010, pp. 163–171. https://doi.org/10.1016/j.memsci.2009.09.033.

[10] Eisenman, G., Sandblom, J. P., and Walker, J. L., "Membrane Structure and Ion Permeation," *Science*, Vol. 155, No. 3765, 1967, pp. 965–974. https://doi.org/10.1126/science.155.3765.965.

[11] Zhurov, K., Dickinson, E. J., and Compton, R. G., "Dynamics of ion transfer potentials at liquid-liquid interfaces," *Journal of Physical Chemistry B*, Vol. 115, 2011, pp. 6909–6921. https://doi.org/10.1021/jp202318y.

[12] Jasielec, J. J., Sokalski, T., Filipek, R., and Lewenstam, A., "Neutral-Carrier Ion-Selective Electrodes Assessed by the Nernst–Planck–Poisson Model," *Analytical Chemistry*, Vol. 87, No. 17, 2015, pp. 8665–8672. https://doi.org/10.1021/acs.analchem.5b00065.

[13] Jasielec, J. J., Mousavi, Z., Granholm, K., Sokalski, T., and Lewenstam, A., "Sensitivity and Selectivity of Ion-Selective Electrodes Interpreted Using the Nernst-Planck-Poisson Model," *Analytical Chemistry*, Vol. 90, No. 15, 2018, pp. 9644–9649. https://doi.org/10.1021/acs.analchem.8b02659.

[14] Flavin, M. T., Freeman, D. K., and Han, J., "Interfacial ion transfer and current limiting in neutral-carrier ion-selective membranes: A detailed numerical model," *Journal of Membrane Science*, Vol. 572, 2019, pp. 374–381. https://doi.org/10.1016/j.memsci.2018.10.065.

[15] Brumleve, T. R., and Buck, R. P., "Numerical solution of the Nernst-Planck and poisson equation system with applications to membrane electrochemistry and solid state physics," *Journal of Electroanalytical Chemistry and Interfacial Electrochemistry*, Vol. 90, No. 1, 1978, pp. 1–31. https://doi.org/10.1016/S0022-0728(78)80137-5.

[16] Chang, H., and Jaffé, G., "Polarization in Electrolytic Solutions. Part I. Theory," *The Journal of Chemical Physics*, Vol. 20, No. 7, 1952, pp. 1071–1077. https://doi.org/10.1063/1.1700669.

[17] Nikonenko, V. V., Kovalenko, A. V., Urtenov, M. K., Pismenskaya, N. D., Han, J., Sistat, P., and Pourcelly, G., "Desalination at overlimiting currents: State-of-the-art and perspectives," *Desalination*, Vol. 342, 2014, pp. 85–106. https://doi.org/https://doi.org/10.1016/j.desal.2014.01.008.

[18] Uzdenova, A., and Urtenov, M., "Potentiodynamic and Galvanodynamic Regimes of Mass Transfer in Flow-Through Electrodialysis Membrane Systems: Numerical Simulation of Electroconvection and Current-Voltage Curve," *Membranes*, Vol. 10, No. 3, 2020. https://doi.org/10.3390/membranes10030049.

[19] Li, G., Townsend, A., Archer, L. A., and Koch, D. L., "Electroconvection near an ion-selective surface with Butler–Volmer kinetics," *Journal of Fluid Mechanics*, Vol. 930, 2022, p. A26. https://doi.org/10.1017/jfm.2021.907.

[20] Kwak, R., Pham, V. S., and Han, J., "Sheltering the perturbed vortical layer of electroconvection under shear flow," *Journal of Fluid Mechanics*, Vol. 813, 2017, p. 799–823. https://doi.org/10.1017/jfm.2016.870.

[21] Kwak, R., Pham, V. S., Lim, K. M., and Han, J., "Shear Flow of an Electrically Charged Fluid by Ion Concentration Polarization: Scaling Laws for Electroconvective Vortices," *Phys. Rev. Lett.*, Vol. 110, 2013, p. 114501. https://doi.org/10.1103/PhysRevLett.110.114501.

[22] Li, G., Townsend, A., Archer, L. A., and Koch, D. L., "Suppression of electroconvective and morphological instabilities by an imposed cross flow of the electrolyte," *Phys. Rev. Fluids*, Vol. 6, 2021, p. 033701. https://doi.org/10.1103/PhysRevFluids.6.033701.

[23] Nikonenko, V. V., Mareev, S. A., Pis'menskaya, N. D., Uzdenova, A. M., Kovalenko, A. V., Urtenov, M. K., and Pourcelly, G., "Effect of electroconvection and its use in intensifying the mass transfer in electrodialysis (Review)," *Russian Journal of Electrochemistry*, Vol. 53, No. 10, 2017, pp. 1122–1144. https://doi.org/10.1134/S1023193517090099.

[24] Mitscha-Baude, G., Buttinger-Kreuzhuber, A., Tulzer, G., and Heitzinger, C., "Adaptive and iterative methods for simulations of nanopores with the PNP–Stokes equations," *Journal of Computational Physics*, Vol. 338, 2017, pp. 452–476. https://doi.org/10.1016/j.jcp.2017.02.072.

[25] Park, J.-W., Kim, C., Park, J., and Hwang, J., "Computational Fluid Dynamic Modelling of Particle Charging and Collection in a Wire-to-Plate Type Single-Stage Electrostatic Precipitator," *Aerosol and Air Quality Research*, Vol. 18, No. 3, 2018, pp. 590–601. https://doi.org/10.4209/aaqr.2017.05.0176.

[26] Lastow, O., and Balachandran, W., "Numerical simulation of electrohydrodynamic (EHD) atomization," *Journal of Electrostatics*, Vol. 64, No. 12, 2006, pp. 850–859. https://doi.org/10.1016/j.elstat.2006.02.006.

[27] He, M., and Sun, P., "Mixed finite element analysis for the Poisson–Nernst–Planck/Stokes coupling," *Journal of Computational and Applied Mathematics*, Vol. 341, 2018, pp. 61–79. https://doi.org/10.1016/j.cam.2018.04.003.

[28] Issa, R., "Solution of the implicitly discretised fluid flow equations by operator-splitting," *Journal of Computational Physics*, Vol. 62, No. 1, 1986, pp. 40–65. https://doi.org/10.1016/0021-9991(86)90099-9.

[29] Hagelaar, G., and Kroesen, G., "Speeding Up Fluid Models for Gas Discharges by Implicit Treatment of the Electron Energy Source Term," *Journal of Computational Physics*, Vol. 159, No. 1, 2000, pp. 1–12. https://doi.org/10.1006/jcph.2000.6445.

[30] Weller, H. G., Tabor, G., Jasak, H., and Fureby, C., "A tensorial approach to computational continuum mechanics using object-oriented techniques," *Computers in Physics*, Vol. 12, No. 6, 1998, pp. 620–631. https://doi.org/10.1063/1.168744.

[31] Holzmann, T., *Mathematics, Numerics, Derivations and OpenFOAM(R)*, Holzmann CFD, 2019. https://doi.org/10.13140/RG.2.2.27193.36960.

[32] Cramer, K. R., and Pai, S. I., *Magnetofluid dynamics for engineers and applied physicists*, McGraw-Hill Book Company, 1973.

[33] Haroun, Y., Legendre, D., and Raynal, L., "Volume of fluid method for interfacial reactive mass transfer: Application to stable liquid film," *Chemical Engineering Science*, Vol. 65, No. 10, 2010, pp. 2896–2909. https://doi.org/https://doi.org/10.1016/j.ces.2010.01.012.

[34] Haroun, Y., Legendre, D., and Raynal, L., "Direct numerical simulation of reactive absorption in gas–liquid flow on structured packing using interface capturing method," *Chemical Engineering Science*, Vol. 65, No. 1, 2010, pp. 351–356. https://doi.org/10.1016/j.ces.2009.07.018.

[35] Bouras, H., Haroun, Y., Philippe, R., Augier, F., and Fongarland, P., "CFD modeling of mass transfer in Gas-Liquid-Solid catalytic reactors," *Chemical Engineering Science*, Vol. 233, 2021, p. 116378. https://doi.org/10.1016/j.ces.2020.116378.

[36] Greenshields, C., and Weller, H., *Notes on Computational Fluid Dynamics: General Principles*, CFD Direct Ltd, Reading, UK, 2022.

[37] Alexander, R., "Diagonally Implicit Runge-Kutta Methods for Stiff O.D.E.'s," *SIAM Journal on Numerical Analysis*, Vol. 14, No. 6, 1977, pp. 1006–1021. https://doi.org/10.1137/0714068.

[38] Kennedy, C. A., and Carpenter, M. H., "Diagonally Implicit Runge-Kutta Methods for Ordinary Differential Equations. A Review," , 2016. URL http://www.sti.nasa.gov.

[39] Jasak, H., "Error Analysis and Estimation for the finite volume method with applications to fluid flows." Ph.D. thesis, Imperial College London, 1996.

[40] D'Alessandro, V., Binci, L., Montelpare, S., and Ricci, R., "On the development of OpenFOAM solvers based on explicit and implicit high-order Runge–Kutta schemes for incompressible flows with heat transfer," *Computer Physics Communications*, Vol. 222, 2018, pp. 14–30. https://doi.org/10.1016/j.cpc.2017.09.009.

[41] Yoon, M., Yoon, G., and Min, C., "On Solving the Singular System Arisen from Poisson Equation with Neumann Boundary Condition," *Journal of Scientific Computing*, Vol. 69, No. 1, 2016, pp. 391–405. https://doi.org/10.1007/s10915-016-0200-2.

[42] Paulo J. Oliveira, R. I. I., "An Improved PISO Algorithm for the Computation of Buoyancy-Driven Flows," *Numerical Heat Transfer, Part B: Fundamentals*, Vol. 40, No. 6, 2001, pp. 473–493. https://doi.org/10.1080/104077901753306601.

[43] Leonard, G. L., Mitchner, M., and Self, S. A., "An experimental study of the electrohydrodynamic flow in electrostatic precipitators," *Journal of Fluid Mechanics*, Vol. 127, 1983, p. 123–140. https://doi.org/10.1017/S0022112083002657.

[44] Schönke, J., "Unsteady analytical solutions to the Poisson–Nernst–Planck equations," *Journal of Physics A: Mathematical and Theoretical*, Vol. 45, No. 45, 2012, p. 455204. https://doi.org/10.1088/1751-8113/45/45/455204.

[45] Schlichting, H., and Gersten, K., *Boundary-Layer Theory*, Springer, Berlin, Heidelberg, 2017. https://doi.org/10.1007/978-3-662-52919-5.

[46] Quoc Hung, L., "Electrochemical properties of the interface between two immiscible electrolyte solutions: Part I. Equilibrium situation and galvani potential difference," *Journal of Electroanalytical Chemistry and Interfacial Electrochemistry*, Vol. 115, No. 2, 1980, pp. 159–174. https://doi.org/https://doi.org/10.1016/S0022-0728(80)80323-8.

[47] Ward, K. R., Dickinson, E. J. F., and Compton, R. G., "Dynamic Theory of Membrane Potentials," *The Journal of Physical Chemistry B*, Vol. 114, No. 33, 2010, pp. 10763–10773. https://doi.org/10.1021/jp102599j.

[48] The MathWorks, I., *Curve Fitting Toolbox*, Natick, Massachusetts, United State, 2020. URL https://www.mathworks.com/products/curvefitting.html.

[49] Bakker, E., Bühlmann, P., and Pretsch, E., "Carrier-Based Ion-Selective Electrodes and Bulk Optodes. 1. General Characteristics," *Chemical Reviews*, Vol. 97, No. 8, 1997, pp. 3083–3132. https://doi.org/10.1021/cr940394a.